

1962

Flow in pump and compressor inlet passages

John Clifford Lysen
Iowa State University

Follow this and additional works at: <https://lib.dr.iastate.edu/rtd>

 Part of the [Mechanical Engineering Commons](#)

Recommended Citation

Lysen, John Clifford, "Flow in pump and compressor inlet passages " (1962). *Retrospective Theses and Dissertations*. 2310.
<https://lib.dr.iastate.edu/rtd/2310>

This Dissertation is brought to you for free and open access by the Iowa State University Capstones, Theses and Dissertations at Iowa State University Digital Repository. It has been accepted for inclusion in Retrospective Theses and Dissertations by an authorized administrator of Iowa State University Digital Repository. For more information, please contact digirep@iastate.edu.

This dissertation has been 63-2988
microfilmed exactly as received

LYSEN, John Clifford, 1931-
FLOW IN PUMP AND COMPRESSOR INLET
PASSAGES.

Iowa State University of Science and Technology
Ph.D., 1962
Engineering, mechanical

University Microfilms, Inc., Ann Arbor, Michigan

FLOW IN PUMP AND COMPRESSOR INLET PASSAGES

by

John Clifford Lysen

A Dissertation Submitted to the
Graduate Faculty in Partial Fulfillment of
The Requirements for the Degree of
DOCTOR OF PHILOSOPHY

Major Subjects: Mechanical Engineering
Aerospace Engineering

Approved:

Signature was redacted for privacy.

In Charge of Major Work

Signature was redacted for privacy.

Heads of Major Departments

Signature was redacted for privacy.

Dean of Graduate College

Iowa State University
Of Science and Technology
Ames, Iowa

1962

TABLE OF CONTENTS

	Page
LIST OF SYMBOLS	iii
INTRODUCTION	1
SURVEY OF THE LITERATURE	5
General	6
Boundary Layer over a Body of Revolution	8
Laminar boundary layer over a body of revolution	9
Stagnation point	14
Turbulent boundary layer	17
Transition point	20
Outer Wall Boundary Layer	23
THEORETICAL ANALYSIS	25
EXPERIMENTAL ANALYSIS	44
RESULTS AND DISCUSSION	57
CONCLUSIONS	81
LITERATURE CITED	83
ACKNOWLEDGMENTS	87
APPENDIX A	88
Development of Laminar Boundary-Layer Equations over a Body of Revolution	88
APPENDIX B	100
Derivation of the Difference Equation for the Stream Function	100
APPENDIX C	104
Full Size Drawing of the Model	104

LIST OF SYMBOLS

A	- Area
A_{annulus}	- Area of an annulus normal to direction of flow
\bar{A}	- Constant in Equation 5
a	- Constant with numerical values defined in the text
b	- Constant with numerical values defined in the text
C_1	- Constant of integration
C_1^*	- Constant in Equation 16
C_f	- Drag coefficient for a flat plate in Equation 16
c	- Constant with numerical value defined in the text
d	- Constant with numerical value defined in the text
\bar{d}	- Energy dissipation in turbulent boundary layer
F	- Functional notation
f	- Functional notation
G	- Functional notation
g	- Wall shearing stress parameter, $g = \tau_o \theta / \mu U$
H	- Momentum thickness parameter, $H = \theta / s^*$
\bar{H}	- Energy thickness parameter, $\bar{H} = \bar{s} / s$
H^*	- Inverse of H
h	- Axial spacing in the difference equation
K	- Second shape factor, $K = \frac{\theta^2}{\nu} \frac{dU}{dx}$
k	- Radial spacing in the difference equation
L	- Total arc length along a body of revolution
l	- Parameter used by Thwaites (24)

- m - Parameter used by Thwaites (24)
- N - Reynolds number with basis for calculation given in text
- N_c - Critical Reynolds number at transition point
- N_{eq} - Reynolds number based on U_{avg} and r_{eq}
- n - Dimensionless coordinate, $n = y/s$
- p - Static pressure
- p_o - Total pressure
- q - Exponent in Prandtl's velocity distribution
- R - Third shape factor, $R = \theta^2 r^2 / \nu$
- r - Radial distance from axis of symmetry
- r_{eq} - Equivalent radius defined by Equation 20A, Appendix A
- r_{max} - Radius to theoretical maximum velocity in an annulus, defined by Equation 21A, Appendix A
- \bar{r} - Dimensionless radial distance, $\bar{r} = r/r_{eq}$
- S - First shape factor, $S = \frac{s^2}{\nu} \frac{dU}{dx}$
- s - Boundary-layer thickness
- s^* - Displacement thickness, $s^* = \int_0^s (1 - \frac{u}{U}) dy$
- \bar{s} - Energy thickness, $\bar{s} = \int_0^s \frac{u}{U} (1 - (\frac{u}{U})^2) dy$
- t - Shearing stress
- t_o - Wall shearing stress
- \bar{t} - Energy of turbulent motion
- U - Free stream velocity adjacent to boundary layer
- U_{avg} - Average-flow velocity through the annulus

- \bar{U} - Dimensionless free stream velocity, $\bar{U} = U/U_{avg}$
- u - Axial velocity
- v - Radial velocity
- x - Axial coordinate measured as arc length along a solid boundary
- \bar{x} - Dimensionless arc length, $\bar{x} = x/r_{eq}$
- x_t - Axial arc distance to transition point
- y - Radial coordinate normal to solid boundary
- Z - Third shape factor, $Z = \theta^2/\nu$
- z - Axial coordinate in Cartesian system, measured from stagnation point
- α - Dimensionless spacing in difference equation
- β - Dimensionless spacing in difference equation
- θ - Momentum thickness, $\theta = \int_0^s \frac{u}{U} (1 - \frac{u}{U}) dy$
- μ - Absolute viscosity
- ν - Kinematic viscosity
- ρ - Density
- ψ - Stream function

INTRODUCTION

In axial-flow compressor and pump design, it is customary to assume a uniform axial-velocity profile at the inlet to the first blade row. In reality, however, the velocity profile tends to be parabolic with a maximum value near the mean diameter of the annular passage and with boundary layers on the annulus walls. Andrews, Jeffs, and Hartley (1) point out that this difference between design and actual conditions means that a substantial portion of the blade height may be operating at incidence angles very different from design incidence. Still, the uniform axial-velocity profile is a useful assumption. If the designer attempts to account for the effects of boundary-layer build-up, the resulting machine will most certainly exhibit these losses and perhaps more.¹

However, when trying to predict off-design performance for a given machine, the uniform velocity assumption is not a good one. A turbomachine is designed to fit one set of operating conditions, e.g., speed, capacity, pressure. The possible infinity of actual operating conditions poses real difficulties in off-design prediction. Some measure of

¹Sandercock, Donald M., Lewis Research Center, Cleveland, Ohio. Axial-flow compressor design. Private communication. 1961.

inlet losses due to boundary-layer build-up must be available for accurate analysis. Serovy and Anderson (2) used blade-element methods to estimate off-design performance of axial-flow compressors assuming uniform-inlet axial velocities. Their method, although successful, required more accurate knowledge of inlet conditions for better prediction. Carter (3), in cascade studies, indicated that the inlet-velocity profile in a cascade had a considerable effect on the vorticity leaving the cascade and, therefore, on losses.

Hatch and Bernatowicz (4) suggested that compressors be designed on the basis of a net flow area, e.g., actual geometric area minus boundary-layer area, since the portion of the blade immersed in the boundary layer contributed little to the rating of the machine.

In studying the off-design performance problem, Serovy and Lysen (5) discussed an iterative procedure. Their method was based on successive improvement of blade-element losses until a solution converged within acceptable limits. To find the deviation and loss parameters for any blade element, it is necessary to know the relative fluid inlet-angle, the blade-row geometry, and a parameter which describes the losses for a given blade element. The blade geometry is, of course, known for a given machine and the loss parameter has been fairly well established for various blade configurations. The fluid inlet-angle cannot be

determined unless the velocity distribution at the entrance to the blade row is known. Serovy and Lysen assumed a uniform axial velocity profile. Knowledge of actual inlet velocity would have made their method more accurate.

The purpose of this study was to investigate the various factors affecting axial velocity profiles in inlets to axial-flow turbomachines, with the view toward improving the off-design performance techniques mentioned above. An inlet section was designed using a cylinder with an elliptical nose, concentrically inserted in a plastic pipe to form an annular section similar to that found in a turbomachine. No blades were used in this simplified model, neither was the nose rotated as is the case in an actual machine. Velocity profiles were measured in this model and compared with a theoretical model describing boundary-layer build-up. A drawing of the model is shown in Appendix C.

The theoretical analysis was made by integrating three separate solutions: boundary layer in a circular pipe, boundary layer over a body of revolution, and potential flow through the annular space formed by the insertion of an elliptical-nosed cylinder in a circular pipe.

It should be mentioned that the effects of a bell-shaped mouth, found in many engineering applications, were not considered in this study. It was felt that if the simplified model could be understood, extension to the

complete inlet could be attempted later. As an example of the complexity of the complete problem, the location of the blunt nose in the bell-mouth could have a profound influence on the velocity characteristics. In addition, the effects of pre-rotation found in an actual machine were not considered. The total problem is complex enough to defy a complete study in one undertaking. Rather, the problem must be approached in steps. This study represents an attempt to take the first step.

SURVEY OF THE LITERATURE

No studies were found which dealt directly with the problem of viscous flow through a passage approximating one which might be found in an axial-flow turbomachine. Therefore it was necessary to consider velocity profiles from the viewpoint of boundary-layer theory. Calculation of boundary-layer parameters requires knowledge of the free-stream velocity immediately adjacent to the boundary layer in order to evaluate boundary conditions for the boundary-layer equation with pressure gradient. The potential-flow solution satisfies this requirement. However, the potential-flow solution is by no means easy to calculate. Since the potential flow must be calculated outside the boundary layer, the boundary-layer thickness must be known. The boundary-layer thickness cannot be calculated without the potential-flow solution. The iterative procedure necessary to solve this problem is discussed in the section on Theoretical Analysis.

The theoretical analysis was made by integrating three separate solutions: potential flow through an annular space with boundary layers on each wall, boundary layer over a body of revolution, and outer-wall boundary layer. The literature survey is broken into three major areas corresponding to each of the three separate solutions. The means

of combining the solutions is discussed in the Theoretical Analysis section.

General

The inlet section for an axial-flow turbomachine usually consists of a bell-shaped mouth with a blunt-nosed rotor concentrically inserted. The blunt nose provides the streamlining necessary to smoothly accelerate the flow into the first blade row. A literature survey reveals that there is no standard method for designing the blunt nose. The bell-mouth is usually designed according to American Society of Mechanical Engineers test codes.

Although considerable work has been done in turbomachine blade analysis, virtually no attention has been focused on the inlet problem, with the exception of centrifugal machine inlets. A number of mathematical analyses have been applied to the shrouding of radial turbomachines. These studies have been concerned with potential-flow casing design. Typical of such studies were the approaches of Vavra (6), Ellis, Stanitz, and Sheldrake (7), Spannhake (8), and Gibbings (9). However, these methods were not applicable to the axial-flow machine and they did not take into account the effects of boundary-layer build-up.

Much work has been done on converging inlet sections. Again, these studies were concerned with nonviscous flow.

Horlock and Lewis (10) considered nonviscous flow through the annular space formed by two concentric cones with intersecting apexes and different cone angles. Woods (11) developed an analytic solution using the hodograph method for two-dimensional flow with curved boundaries. Carrier (12) considered accelerating flow in a two-dimensional curved elbow. It is noteworthy to mention that a great body of literature exists on the nonviscous flow through channels and around bodies of various shapes. Effort in this area was particularly intensive during the period 1948-1952. However, this body of literature was not of assistance. Many of the solutions were too highly specialized to be of general use. It was decided to evaluate the potential flow using numerical techniques.

Several studies were undertaken to determine the effect of placing a body in a wind tunnel. Abdurahiman (13) predicted the effects of compressibility in two-dimensional channel flow. Emmons (14) performed similar calculations for an airfoil in a wind tunnel and in a free air-stream. Neither of these studies dealt with the problem of boundary-layer build-up, however.

Turbomachine inlet testing was dealt with by many workers. The approach used was to measure the overall losses incurred in a given inlet. The results were usually given in the form of a blockage factor, i.e., the ratio of

actual flow to isentropic flow conditions. No mention was made of actual velocity profiles. Experimental work along these lines has been done by Sacks and Spreiter (15), Ruden (16), and Nichols and Rinkoski (17).

The only work found which dealt with actual inlet-velocity profiles was done by Sega and Yokoyama (18). They performed systematic measurements of inlet-velocity profiles for inlets of various configuration. No attempt was made to perform a theoretical analysis. Their results were used later in this study for comparison purposes.

For this study air at low velocities was used as a working fluid. Incompressible flow was assumed. Johnston (19) in tests on inlet conditions for axial-flow turbo-machines (only static-pressure losses were considered) showed that at a Reynolds number of about $2.5(10)^5$ and an inlet Mach number of 0.15, incompressible flow could be assumed with negligible error. Dean (20) wrote the steady-flow energy equation in terms of the Mach number. By using a series expansion he showed that the incompressible flow assumption was valid up to a Mach number of 0.2 with less than one per cent error.

Boundary Layer over a Body of Revolution

In considering the boundary-layer development over a body of revolution, several distinct aspects of the problem

were considered. First, laminar boundary layer over a blunt body was investigated. In this study an elliptical nose was used. As will be discussed later, mathematical discontinuities occurred at the stagnation point of the elliptical nose. These discontinuities required special treatment of the boundary layer at the stagnation point. The second portion of this section deals with the stagnation point. Thirdly, it was possible that the flow would not remain entirely laminar. Therefore a discussion of turbulent boundary layer was included. Finally, the ability to calculate the turbulent boundary layer depended on knowledge of the transition point from laminar to turbulent flow. This subject was also treated separately.

Laminar boundary layer over a body of revolution

Schlichting (21) reported a two-dimensional approximate solution based on the work of Pohlhausen. A detailed discussion of this solution was included in Appendix A. The final result of these calculations took the following form, where x is the arc length along the solid boundary, and C_1 is zero for a flat plate.

$$\frac{U\theta^2}{\nu} = \frac{0.470}{U^5} \int_{x=0}^x U^5 dx + C_1 \quad (\text{Eq. 1})$$

If the free-stream velocity distribution is known, Equation 1

may be integrated to give the momentum thickness, θ , directly. Other parameters of interest such as the boundary-layer thickness, s , and the displacement thickness, s^* , may be determined in the manner discussed in Appendix A.

Equation 1 can be extended to a body of revolution following the approach taken by Rott and Crabtree (22). The details of this transformation were also presented in Appendix A. The resulting equation took the form

$$\frac{U\theta^2}{\nu} = \frac{0.470}{r^2 U^5} \int_{x=0}^x r^2 U^5 dx + C_1 \quad (\text{Eq. 2})$$

Equation 2 was transformed into nondimensional form, using the equivalent radius defined by Knudsen and Katz (23) and an average velocity. (See the list of symbols for definitions and Appendix A for derivation of the equation.)

$$\left(\frac{\theta}{r_{\text{eq}}}\right)^2 N_{\text{eq}} = \frac{0.470}{r^2 U^6} \int_{\bar{x}=0}^{\bar{x}} r^2 U^5 d\bar{x} + C_1 \quad (\text{Eq. 3})$$

N_{eq} is the Reynolds number based on the average annulus velocity and the equivalent radius. In its final form Equation 3 demonstrated that the momentum-thickness distribution depended on the Reynolds number as well as the potential flow. This particular fact complicated the problem since numerous calculations were necessary for each value of

Reynolds number. This problem was discussed at length in the section on Theoretical Analysis.

Thwaites (24) synthesized the solutions of Pohlhausen, Falkner and Skan, Howarth, and Hartree. Thwaites employed two arbitrary parameters, l and m ,

$$\left(\frac{\partial u}{\partial y}\right)_{y=0} = \frac{U_l}{\theta} ; \quad \left(\frac{\partial^2 u}{\partial y^2}\right)_{y=0} = \frac{U_m}{\theta^2} .$$

He obtained values for $H = \theta/s^*$ and l as functions of m and plotted these values for the several cases mentioned above. By making the assumption that

$$F(m) = a - bm,$$

Thwaites showed that

$$\frac{U\theta^2}{\nu} = \frac{0.45}{r^2 U^5} \int_{x=0}^x U^5 dx + C_1 .$$

Rott and Crabtree (22) showed that the functions $H(m)$ and $l(m)$ developed by Thwaites were applicable to the axially-symmetric case and derived an equation of the same form as Equation 2 but with a different constant,

$$\frac{U\theta^2}{\nu} = \frac{0.45}{r^2 U^5} \int_{x=0}^x r^2 U^5 dx + C_1 . \quad (\text{Eq. 4})$$

Truckenbrodt (25) started with the energy equation which was derived using the method of moment-integrals. The energy equation resulted when the momentum equation was multiplied by u^p and p set equal to one. Truckenbrodt utilized an energy-thickness parameter, $\bar{H} = \bar{s}/s$, based on the energy thickness, \bar{s} . (See List of Symbols for the definition of \bar{s} .) He assumed that a definite relation existed between \bar{H} and the momentum-thickness parameter, $H = \theta/s^*$. By integrating the energy equation, Truckenbrodt derived the following,

$$\left(\frac{U\theta}{\nu}\right)^q \theta = \frac{C_1 + \bar{A} \int_{x_1}^x U^{3+2q} r^{1+q} dx}{U^{3+2q} r^{1+q}} \quad . \quad (\text{Eq. 5})$$

This equation, Truckenbrodt pointed out, was valid for both laminar and turbulent flow. For laminar flow $C_1 = 0$, $\bar{A} = 0.441$, and $q = 1$. (The turbulent-flow case will be discussed later.)

Loitsianskii (26) also employed the method of moment-integrals, but used three equations corresponding to multiplying the momentum equation by y^p with $p = 0, 1, 2$. He devised a method for solving the three equations simultaneously in terms of three parameters,

$$K = \frac{U\theta^2}{\nu}, \quad g = \frac{t_o \theta}{\mu U}, \quad H^* = \frac{s^*}{\theta} \quad .$$

By assuming similar velocity profiles for a flat plate, he developed the expression

$$\frac{U\theta^2}{\nu} = \frac{0.44}{U^{4.5}} \int_{x=0}^x U^{4.5} dx + C_1 . \quad (\text{Eq. 6})$$

Wright and Bailey (27) assumed that $H = \text{constant}$ and derived the equation

$$\frac{U\theta^2}{\nu} = \frac{0.44 x}{U} + C_1 . \quad (\text{Eq. 7})$$

The method of Rott and Crabtree (22) mentioned previously could be used to transform Equations 6 and 7 to the case of a body of revolution.

It should be noted that Equations 2, 4, 5, 6, and 7 gave values of the parameter $U\theta^2/\nu$ as a function of U and x . Five different approaches were represented and all showed a remarkable degree of similarity. For purposes of this study, Waltz' approximation of Pohlhausen's solution, Equation 1, as modified by the method of Rott and Crabtree, Equation 3, was selected.

Millikan (28) also studied the boundary layer over a body of revolution. He transformed the boundary-layer equations into cylindrical coordinates and included a pressure gradient term. He assumed a parabolic velocity profile

which obviated the necessity for using a shape factor such as that used by Pohlhausen. By integrating the momentum equation Millikan derived an expression for the boundary-layer thickness

$$\frac{s^2 U}{\nu} = \frac{30}{r^2 U^8} \int_0^x r^2 U^8 dx + C_1 .$$

When his parabolic velocity profile was substituted in the definition of the momentum thickness, $\theta/s = 4/225$,

$$\frac{\theta^2 U}{\nu} = \frac{0.533}{r^2 U^8} \int_0^x r^2 U^8 dx + C_1 . \quad (\text{Eq. 8})$$

Because of the difference in velocity exponents, it was not possible to compare Millikan's equation with those previously discussed. However, it may be noted that Millikan's selection of a parabolic velocity profile corresponded to the assumption that H was constant since the velocity profile did not contain a shape factor. This assumption was not satisfactory for our purposes.

Stagnation point

As was mentioned previously, special attention must be focused on the stagnation point because of mathematical discontinuities at the elliptical nose. If we consider Equation 15A, Appendix A,

$$\frac{dZ}{dx} = \frac{1}{U} \left(F(K) - 2K \frac{1}{r} \frac{dr}{dx} \frac{U}{U'} \right), \quad K = ZU'.$$

For the case of a blunt nose, Schlichting (21) suggested that

$$\lim_{x \rightarrow 0} \left(\frac{1}{r} \frac{dr}{dx} \frac{U}{U'} \right) = 1.$$

When this value was substituted in Equation 15A and $dz/dx = 0$, Equation 15A reduced to

$$F(K) - 2K = 0. \quad (\text{Eq. 9})$$

Schlichting solved this equation and calculated the values $S_0 = 1$ and $K_0 = 0.05708$. Using the definition of K ,

$$Z_0 U'_0 = 0.05708,$$

or, substituting the definition of Z ,

$$\frac{\theta^2 U'_0}{\nu} = 0.05708. \quad (\text{Eq. 10})$$

Millikan (28) proposed that a blunt nose be considered spherical in the neighborhood of the stagnation point. He used this assumption because the potential flow over a sphere was easily expressed as $U = 1.5 U_\infty r_0 \sin \theta$ with

$\theta = 0$ at the stagnation point. Using a limiting process, Millikan concluded that

$$\frac{s^2 U}{r_o v} = 1.818 .$$

If Millikan's parabolic velocity profile is substituted,

$$\frac{\theta^2 U}{r_o v} = 0.0323 . \quad (\text{Eq. 11})$$

Millikan's sphere assumption was applied to Equation 10. Near the stagnation point, $\sin \theta \doteq \theta$, and $x \doteq r_o \theta$, then $dU/dx \doteq 1.5 U_\infty / r_o$. Putting this value in Equation 10,

$$\frac{\theta^2 U_\infty}{r_o v} = 0.0381 . \quad (\text{Eq. 12})$$

Tomotika as quoted by Knudsen and Katz (23, p. 309) performed actual measurements on a sphere and verified Millikan's potential-flow assumption. Tomotika presented his results for the boundary layer over a sphere in the form of an empirical equation. When this equation was evaluated at the stagnation point, a value different from Millikan's resulted. Tomotika's equation gave

$$\frac{U_\infty s^2}{r_o v} = 3.15 .$$

Tomotika used the same velocity profile form that Pohlhausen employed. If Schlichting's value of $S_0 = 4.716$ is substituted in the equation defining momentum thickness, the momentum thickness becomes, $\theta = 0.11s$. Substituting this value in Tomotika's equation,

$$\frac{U_\infty \theta^2}{r_0 \nu} = 0.0381 . \quad (\text{Eq. 13})$$

This value agreed very well with Schlichting's value modified for flow over a sphere, Equation 12.

If Equation 13 is rewritten in the form of Equation 3, a more useful form results.

$$\left(\frac{\theta}{r_{eq}}\right)^2 N_{eq} = 0.0381 \left(\frac{r_0}{r_{eq}}\right) \left(\frac{U_{avg}}{U_\infty}\right)$$

In this form r_0 is the radius of curvature of the blunt nose at the stagnation point. The value thus obtained becomes the constant of integration, C_1 , in Equation 3.

Turbulent boundary layer

Millikan (28) approached the turbulent boundary-layer problem in a manner similar to his laminar boundary-layer analysis. In the case of a turbulent boundary layer, however, he used the Prandtl velocity distribution

$$\frac{u}{U} = \left(\frac{y}{s}\right)^{\frac{1}{q}} .$$

Based on Nikuradse's flat plate data, Millikan chose $q = 7$. Millikan pointed out that the shearing stress is completely determined by the assumed velocity distribution. With the above distribution, Millikan reported the wall shearing stress calculated by von Kármán as

$$\frac{t_o}{\rho} = 0.0225 U^2 \left(\frac{y}{Us}\right)^{\frac{1}{4}} .$$

Using these values in the momentum-integral equation, he obtained

$$\frac{115}{U^{28}} \frac{35}{r^{28}} \frac{5}{s^4} \Big|_{x_t}^x = 0.289 \nu^{\frac{1}{4}} \int_{x_t}^x U^{\frac{108}{28}} r^{\frac{35}{28}} dx . \quad (\text{Eq. 14})$$

Truckenbrodt (25) developed an expression for the turbulent boundary layer based on the energy equation. Rather than working with the shearing stress, as is done when using the momentum equation, Truckenbrodt used an energy dissipation relation which is related to the shearing stress.

$$\frac{\bar{d} + \bar{t}}{\rho U^3} = \int_0^s \frac{t}{\rho U^3} \frac{\partial}{\partial y} \left(\frac{u}{U}\right) dy$$

This quantity represents the dimensionless friction work performed in the boundary layer by the shearing stress. The quantity, \bar{d} , represents heat generated by shearing stresses dissipated as internal energy and the quantity, \bar{e} , is the energy of turbulent motion. Truckenbrodt assumed that \bar{e} could be neglected when compared to \bar{d} . When $\bar{d}/\rho U^3$ was plotted against Reynolds number based on momentum thickness, for various values of H , the resulting curves were almost independent of H . Truckenbrodt assumed, therefore, that

$$\frac{\bar{d}}{\rho U^3} = \frac{0.56 (10)^{-2}}{\left(\frac{U\theta}{\nu}\right)^{1/6}} .$$

A simplified integral equation resulted.

$$\theta \left(\frac{U\theta}{\nu}\right)^q = \frac{C_1 + \bar{A} \int_{x_t}^x U^{3+2q} r^{1+q} dx}{U^{3+2q} r^{1+q}} \quad (\text{Eq. 15})$$

The quantity, x_t , is the transition point from laminar to turbulent flow. Truckenbrodt further assumed that the momentum thickness can be expressed in terms of the drag coefficient for a rough flat plate, C_f .

$$\frac{\theta}{L} = \frac{[C_1^* + (\frac{C_f}{2})^{1+q} \int_{x_t/L}^{x/L} (\frac{U}{U})^{3+2q} (\frac{r}{L})^{1+q} d(\frac{x}{L})]^{1/q}}{(\frac{U}{U})^3 (\frac{r}{L})}$$

(Eq. 16)

$$C_1^* = [\frac{C_f}{2} (\int_0^{x_t/L} (\frac{U}{U})^5 (\frac{r}{L})^2 d(\frac{x}{L}))^{1/2}]^{1+q}$$

If the flow is laminar, $q = 1$, and if the flow is turbulent, $q = 1/6$. The quantity, L , is the total arc length of the body of revolution. If the flow is entirely turbulent from the leading edge, $x = 0$, then $C_1^* = 0$.

Transition point

The transition point from laminar to turbulent flow is probably the most difficult problem encountered in boundary-layer theory. Little is known about the mechanism of transition and still less is known about the actual transition point itself. Very few data for determining the transition point are available. There are two general methods commonly used to handle this problem.

The first method, according to Millikan (28), assumed that the transition from laminar to turbulent flow took place instantaneously rather than through a region. Under this assumption both the laminar and turbulent boundary

layers are calculated from the leading edge. When a critical Reynolds number is reached (based on boundary-layer thickness), instantaneous transition takes place. Millikan showed that this hypothesis led to a discontinuity in the boundary-layer thickness. For example, using the Blasius profiles for a flat plate, the turbulent thickness was 1.27 times the laminar thickness. Millikan showed that the same sort of discontinuity applied to a body of revolution. In the transition region, however, the flow character changed continuously from laminar to turbulent flow. The wall shearing stress also changed continuously and smoothly. If there were not a discontinuity in the boundary-layer thickness, there would be a discontinuity in the wall shearing stress. Millikan pointed out that the excellent agreement between theory and experiment on a flat plate indicated that the discontinuity in boundary-layer thickness was approximately the correct one in order to give a smoothly increasing value of wall shearing stress.

The second method, proposed by Truckenbrodt (25), matched up laminar and turbulent momentum thickness at the transition point. At some critical Reynolds number transition is assumed to occur instantaneously. The turbulent boundary layer is calculated on the basis of some fictitious length such that the momentum thickness is the same as that of the laminar boundary layer at the point of transition.

This approach implies a discontinuity in wall shearing stress. Truckenbrodt expressed this discontinuity as a function of a change in the shape parameter H .

The main problem is not the selection of method, but of critical Reynolds number, N_c . N_c depends on initial turbulence and increases as initial turbulence decreases. Millikan (28) gave lower limit values of N_c for pipes where N_c was calculated using the tube diameter. These values varied from 1160 to 1650. He further indicated that the upper limit was uncertain but was of the order of 12,000.

Schlichting (21) pointed out that at medium Reynolds number, $(10)^5$ to $(10)^6$, based on chord length for airfoils, the transition point occurred slightly behind the point of minimum pressure regardless of shape. He further pointed out that a decrease in pressure, accelerating flow, had a stabilizing effect.

In a systematic investigation of transition points for Joukovsky airfoils, Bussmann and Ulrich (29) demonstrated that the transition point always occurred behind the point of minimum pressure regardless of Reynolds number.

The pressure minimum in this study occurred at the joining of the elliptical nose to the cylinder or perhaps behind it. Therefore, it was assumed on the basis of the above results that the transition point occurred in the straight annulus section.

Outer Wall Boundary Layer

For the cylindrical section up to the tip of the blunt nose, it was assumed that $s \ll D$. Using this assumption, the boundary-layer thickness could be calculated using flat-plate theory. From the blunt nose back, the outer wall was influenced by a pressure gradient and the methods previously discussed applied.

In this study the cylindrical section was preceded by a bell-mouth leading out of a large settling chamber. In order to use the flat plate assumption, it was necessary to replace the bell-mouth by an equivalent length of flat plate which would give the same boundary-layer thickness as that produced by the bell-mouth.

Rivas and Shapiro (30) have studied boundary layer build-up in a bell-mouth. Based on a potential-flow solution, they used the method of Thwaites (24) as modified by Rott and Crabtree (22) to calculate the boundary layer. Their work was done on a standard American Society of Mechanical Engineers bell-mouth. A similar bell-mouth was used in this study. Therefore, the calculations of Rivas and Shapiro can be used directly to estimate the thickness of the boundary layer at the entrance to the cylindrical section. The flat-plate data of Knudsen and Katz (23) were applied to the pipe.

Prandtl and Tietjens (31) reported Nikuradse's extensive studies on velocity profile development in cylindrical pipes. They plotted u/U versus x/rN for various radial positions y/r . Again using the method of Rivas and Shapiro (30) to replace the bell-mouth by an equivalent length of pipe, the data presented by Prandtl and Tietjens could be compared with the flat-plate assumption.

THEORETICAL ANALYSIS

One boundary condition used in evaluating boundary-layer parameters requires knowledge of the free-stream velocity at the outside edge of the boundary layer (when $y = s$, $u = U$). The velocities obtained from the potential-flow solution satisfy this requirement. Obtaining the potential-flow solution in a closed duct is not a simple problem, however, due to the fact that the potential-flow equation and the boundary-layer equation are coupled. Therefore, an iterative solution results. The potential-flow solution is calculated assuming a zero-thickness boundary layer. From this solution a boundary-layer thickness distribution can be calculated. A new potential-flow solution can then be calculated based on the original area minus the boundary-layer area. The process is continued until the solution converges to some acceptable accuracy.

In this study the potential-flow solution was calculated initially assuming zero-thickness boundary layers on both the inside and outside walls. The potential solution was determined by numerically evaluating the stream function. (See Appendix B for the derivation of the difference equation for the stream function in cylindrical coordinates.) The solid boundaries were arbitrarily assigned values. At a sufficient distance upstream and downstream of the blunt

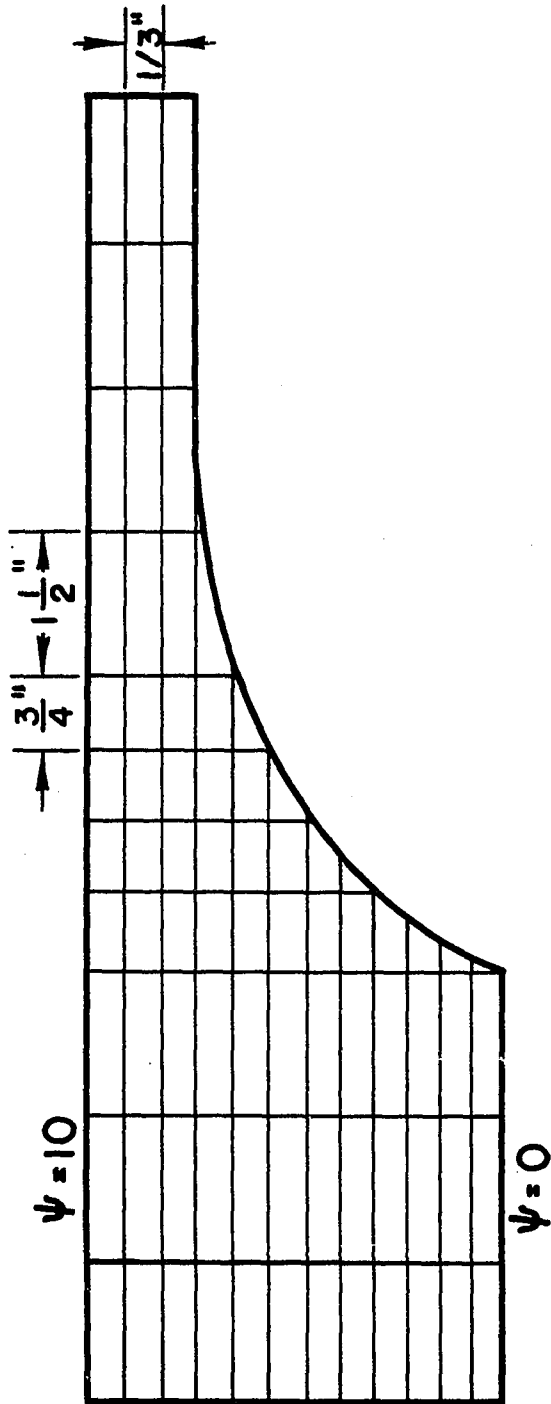
nose, the flow was assumed to be uniform and was broken into equal flow areas. The streamlines bounding these equal areas were assigned values. For example, ahead of the blunt nose the stream function was expressed as

$$\psi = \psi_{\text{outer wall}} \left(\frac{r}{r_{\text{outer wall}}} \right)^2.$$

The interior region was divided into a series of mesh-points as shown in Figure 1. Unequal spacing was used to more clearly define the stream function near the region of large curvature. A system of sixty-one equations resulted. The system of equations was solved using the matrix inversion program of the Iowa State University Statistical Laboratory on an IBM 650 computer.

After values of the stream function were known at the interior mesh-points, a curve of stream function value versus radial distance was plotted at a given value of axial distance. This curve was graphically differentiated at various values of radial distance. By plotting the resulting derivatives versus radial distance from the solid boundary, the axial velocity components at both the inner and outer wall were determined by extrapolation. The whole process was repeated for several different axial-distance values. The resulting values were plotted against axial

Figure 1. Mesh used in calculating stream function



distance and a smoothed curve drawn. The derivatives obtained by graphical differentiation were checked using a four-point finite-difference approximation for the stream function near the walls. The resulting equation was differentiated and the values obtained in this way agreed very well with those obtained by graphical means.

In order to determine the radial component of velocity, curves of stream-function value versus axial distance for various radial values were graphically differentiated in the manner described above. A smoothed curve of radial velocity component was plotted.

The velocity components from the smoothed curves were then combined vectorially. Near the nose the method used introduced some inaccuracies. However, since the main purpose for determining velocities was to integrate the momentum-thickness distribution, Equation 3, these errors were not serious. In Equation 3 the velocities were expressed as a dimensionless ratio less than one. This ratio is raised to the fifth power and the ratios near the nose contribute very little to the integral further back. This study is primarily concerned with the rear portion of the blunt nose since this is the area where the blades of an axial turbomachine would be mounted.

An approximate method for determining velocities was also attempted and checked with the more accurate solution

outlined above. The approximate method assumed one-dimensional flow and, therefore, velocities were simply expressed as an area ratio.

$$U = U_{\text{avg}} \left(\frac{A_{\text{annulus}}}{A} \right)$$

Over the inner wall or body of revolution, deviation was most pronounced near the nose and became less in the region further back. The velocity distribution for the outer wall showed good agreement. The approximate velocity distribution along with those obtained by the more accurate method described above are shown in Figure 2.

The velocities thus obtained were used to calculate the momentum-thickness distribution by integrating Equation 3. It should be mentioned that inaccuracies in evaluating the potential velocity by differentiating the stream function were partially eliminated by the integration which tended to smooth out errors. The trapezoidal rule was used to perform the integration. The results for the body of revolution are shown in Figure 3. The calculations for the outer wall will be discussed later, although the method described below for determining the boundary-layer thickness is applicable.

By using the methods described in Appendix A, the parameter, $K = (\theta/r_{\text{eq}})^2 N_{\text{eq}} d\bar{U}/d\bar{x}$, was calculated. The values of K were applied to Table 12.2 in Schlichting (21)

Figure 2. Dimensionless velocity distribution on inner and outer walls

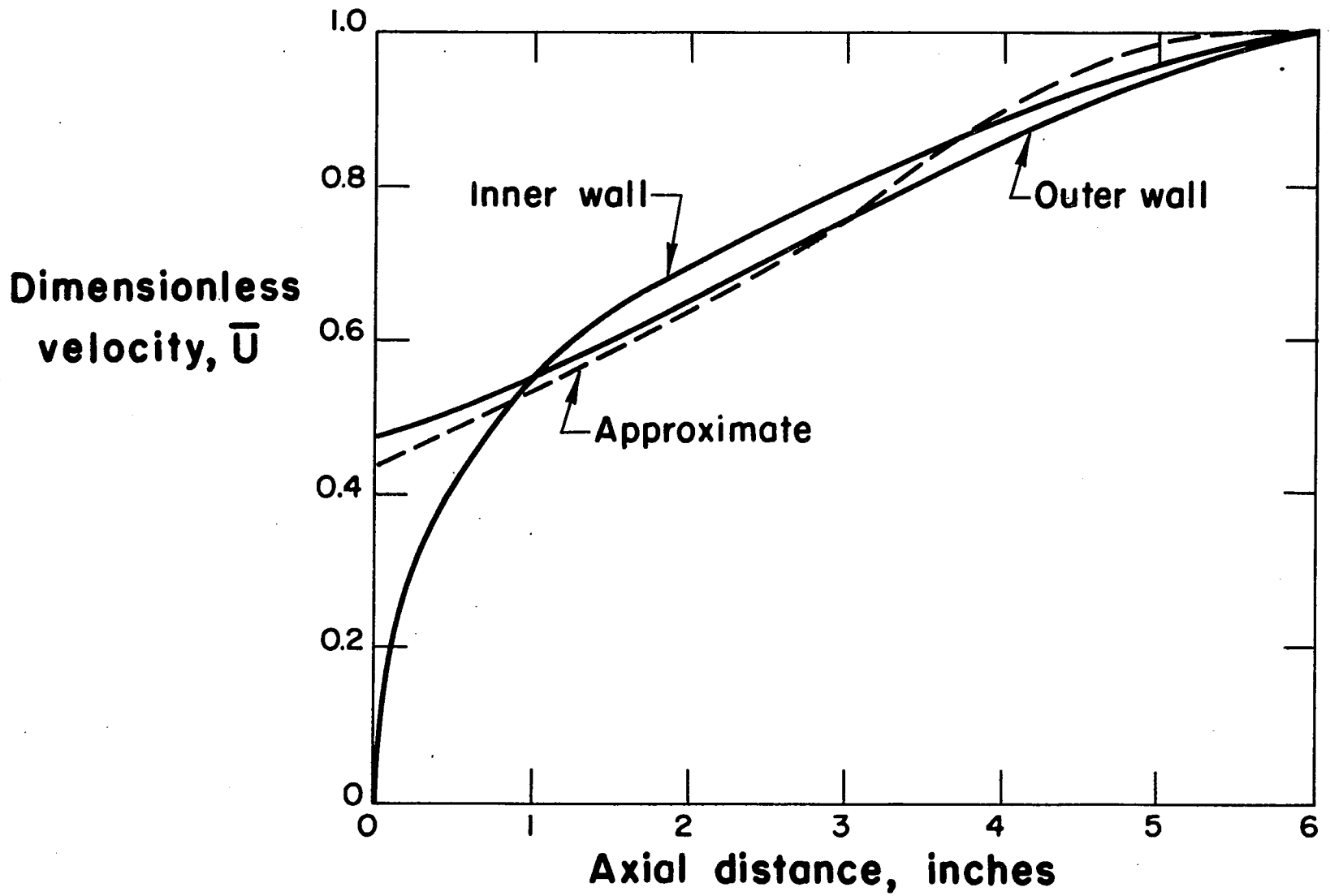
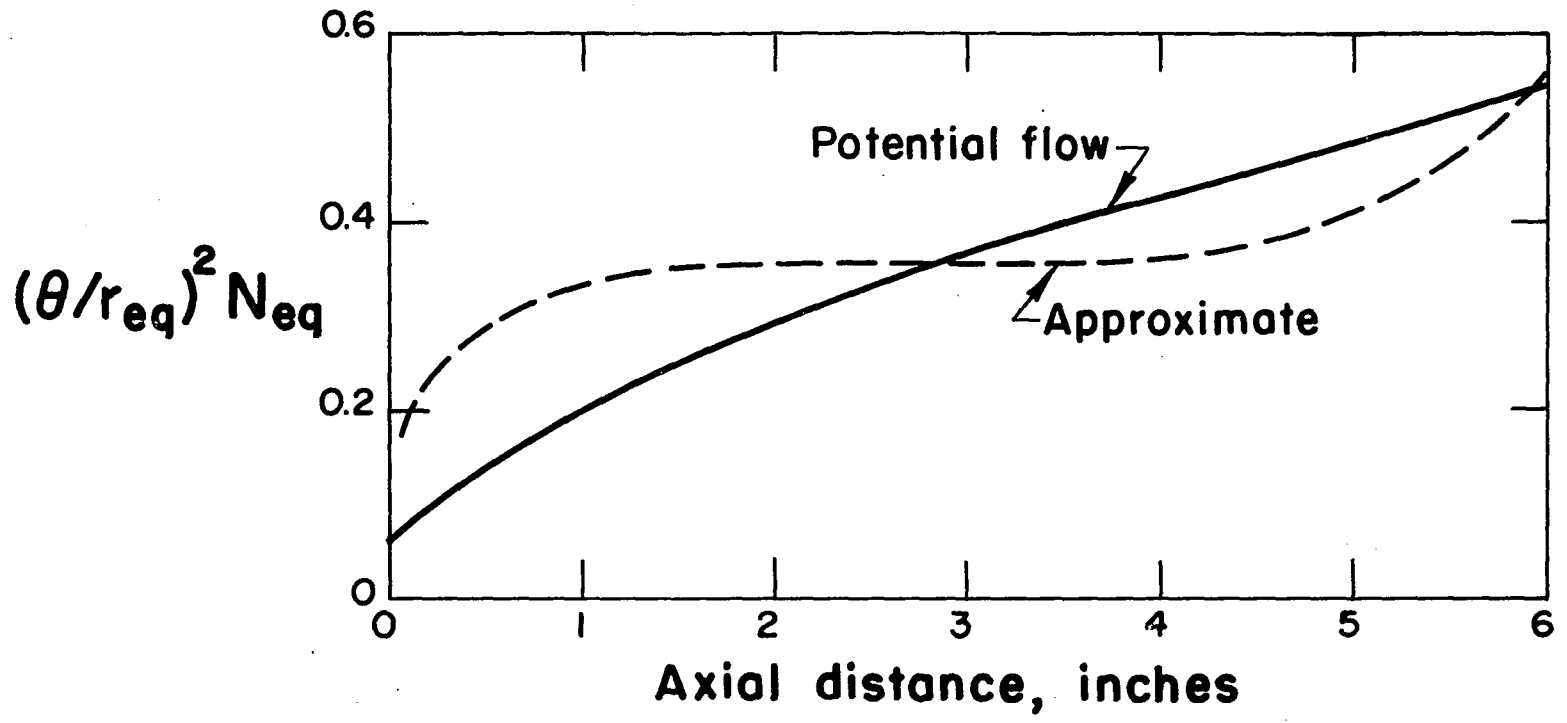


Figure 3. Momentum thickness distribution over the body of revolution



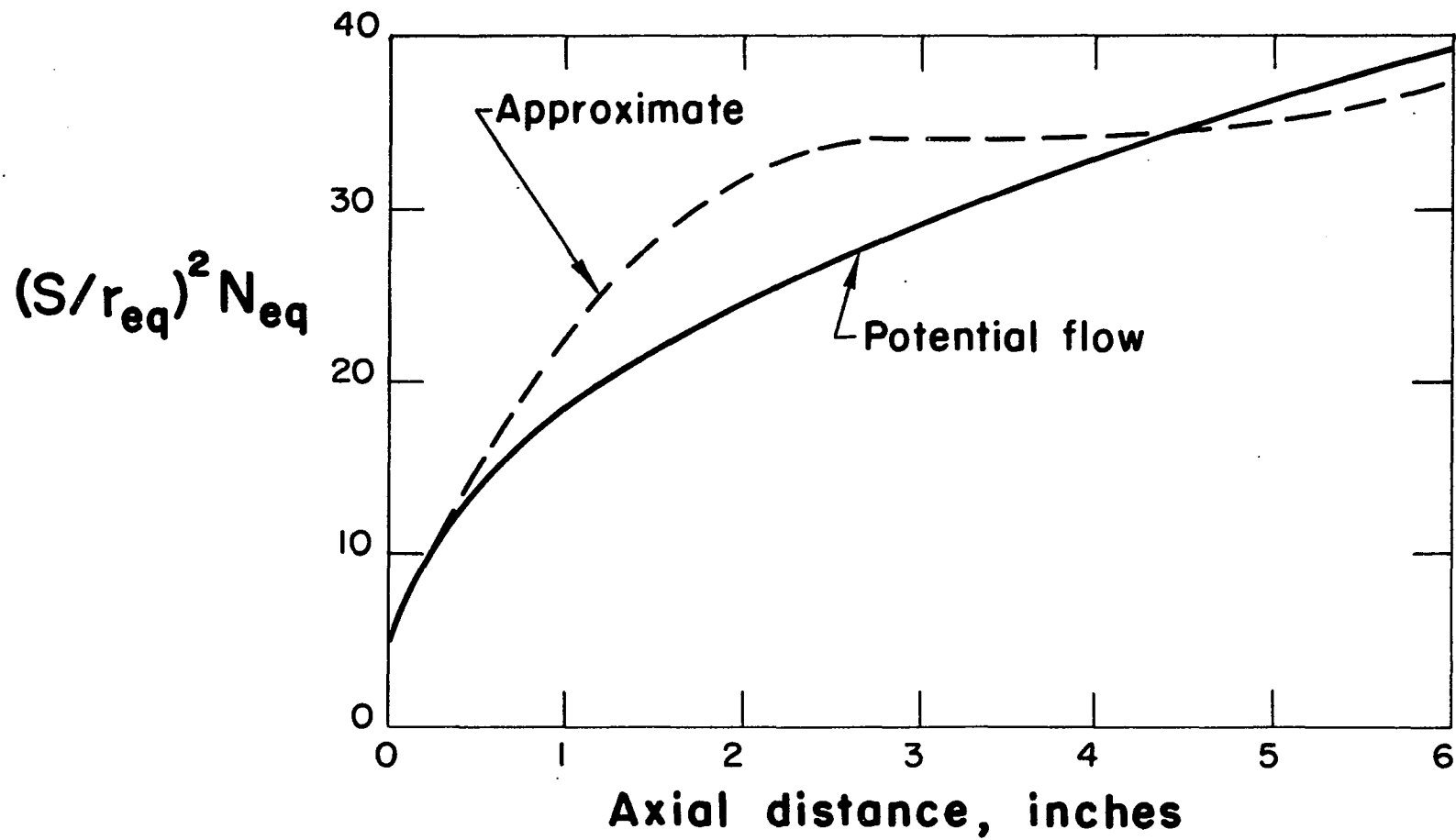
to determine the boundary-layer-thickness distribution which is shown in Figure 4 for the body of revolution. At the stagnation point it was assumed that the potential flow behaved as if the nose were spherical, with the radius of the sphere equal to the radius of curvature of the elliptical nose. Using this assumption it was possible to evaluate $d\bar{U}/d\bar{x} = 0.835$ at the stagnation point.

As was mentioned previously, the iterative procedure is exceedingly cumbersome since it must be performed for each individual value of Reynolds number which is of interest. In order to perform a second iteration, a specific Reynolds number was selected ($N_{eq} = 61,500$). The results of this iteration using the approximate velocity distribution are shown in the next section with the experimental results for flow at the same Reynolds number (Figure 9).

It should be noted that the boundary layer over the body of revolution is of the order of 0.01 inch or less for $N_{eq} = 100,000$ or greater. For $N_{eq} = 10,000$ the boundary-layer thickness is of the order of 0.1 inch in a passage of one inch. From this it may be concluded that the boundary layer over the body of revolution need not be considered for flow at high Reynolds numbers.

An attempt was made to calculate the boundary layer through the bell-mouth and pipe with the flat-plate data of

Figure 4. Dimensionless boundary layer thickness distribution over the body of revolution



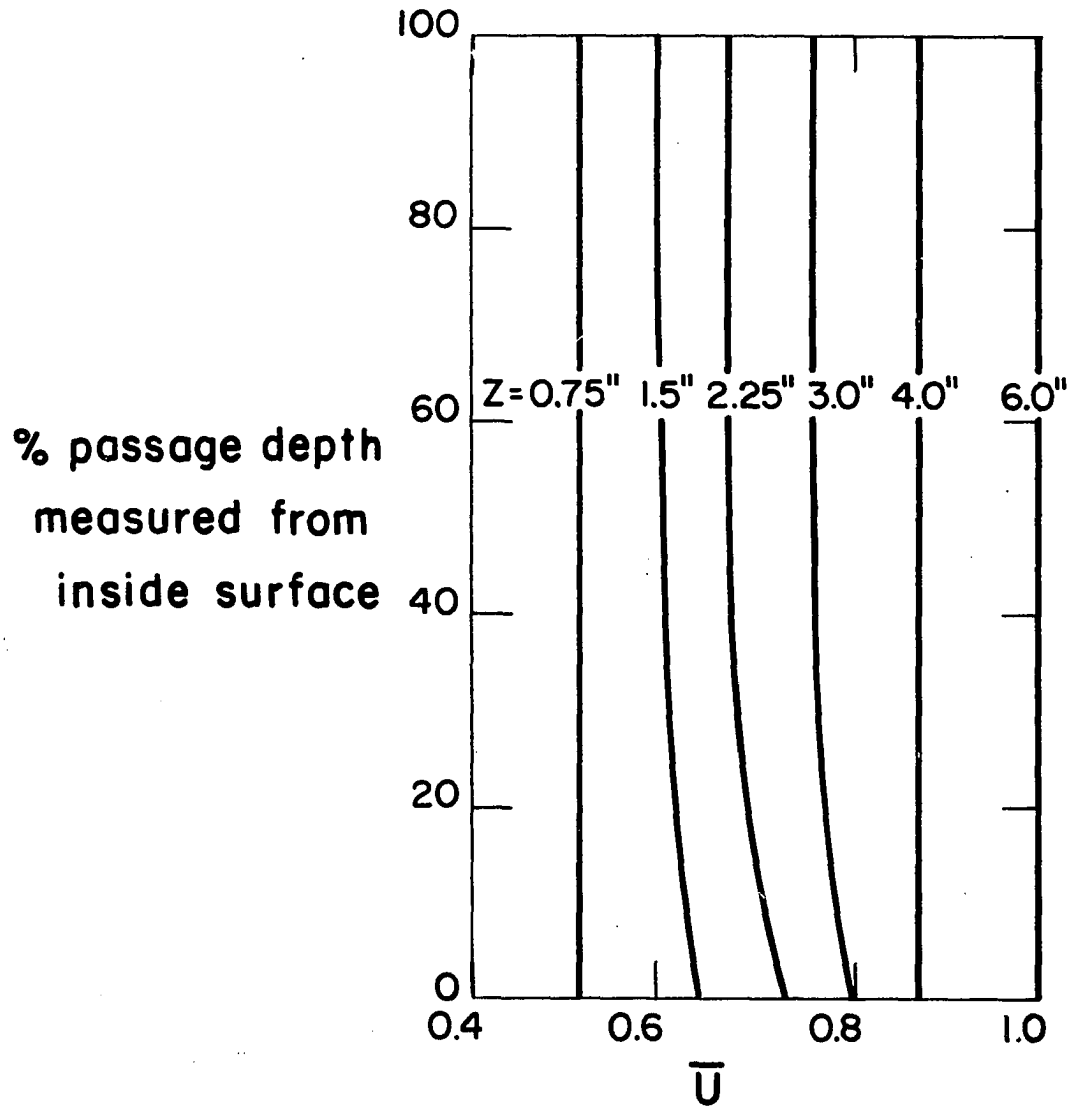
Knudsen and Katz (23) using an equivalent length of flat-plate for the bell-mouth from the data of Rivas and Shapiro (30). The results obtained from these calculations were excessively large. This was perhaps due to the fact that the boundary layer in a pipe is confined whereas the boundary layer on a flat plate is free to expand. Therefore, the initial value of the boundary layer on the outer wall opposite the stagnation point was determined experimentally and this value used as a constant of integration in Equation 3.

It should be noted that the approximate velocity distribution checks out very well with the more accurate potential-flow solution near the outer wall. Use of the approximate solution is completely justified for calculating the outer-wall boundary layer.

At high Reynolds numbers ($N_{eq} = 100,000$) the boundary layer thickness over the body of revolution, as was mentioned before, became negligible when compared to the passage dimension. If the boundary layer on the outer wall is also negligible, the velocity profile can be determined by the initial potential velocity distribution since additional iterations will not appreciably alter the initial potential-flow solution. The velocity profiles calculated using this assumption are presented in Figure 5.

The complete calculation procedure, based on the

Figure 5. Velocity profiles at high Reynolds number with negligible outer wall boundary layer



foregoing comments, is presented in the following summary.

Case 1. Blockage factor. If only a blockage factor is desired, the potential-flow solution is not necessary. The momentum-thickness distribution can be calculated with the approximate velocity distribution. From the momentum thickness, the boundary-layer thickness can be determined in the manner discussed previously. The whole process can be iterated until the solution converges. From the final momentum-thickness distribution, the displacement thickness can be determined. Since the displacement thickness is a measure of "lost flow," blockage can be determined directly.

Case 2. Large Reynolds number, boundary layer over body of revolution is negligible, boundary layer on outer wall is finite. From experimental work or from a study such as that of Rivas and Shapiro (30) for a bell-mouth inlet, determine the momentum thickness of the outer-wall boundary layer at a point on the wall opposite the stagnation point. This value is a constant of integration to be added to the value obtained from integrating Equation 3. Calculate the momentum thickness distribution using Equation 3 and the approximate velocity distribution. Calculate the boundary-layer thickness. Iterate using the original flow area reduced by the boundary-layer area until a solution converges. Based on the passage represented by the solid boundaries reduced by the final boundary-layer thickness, calculate the

potential-flow solution and calculate the velocity profile from it.

Case 3. Large Reynolds number, boundary layer over body of revolution is negligible, boundary layer on outer wall is negligible. Compute the potential-flow solution and determine velocity profiles from it.

Case 4. Small Reynolds number. Using the approximate velocity distribution, calculate the momentum-thickness distribution for the outer and inner wall. Previous remarks about outer wall mentioned in Case 2 are applicable. Calculate the boundary-layer thickness and iterate until a solution converges. Based on these boundary-layer thicknesses, calculate the potential-flow solution. From the potential-flow solution, determine the momentum-thickness distribution on the inner and outer walls and check with that calculated by the approximate velocity distribution. If these values do not agree within acceptable limits, compute a new potential-flow solution based on the boundary-layer thickness calculated by the first potential-flow solution. When the solution converges, compute the velocity profiles from the potential-flow solution.

Case 5. Velocity profile over forward portion of nose. The previous cases assumed that velocity profiles were to be calculated over the rear portion of the nose where the approximate velocity distribution compares favorably with

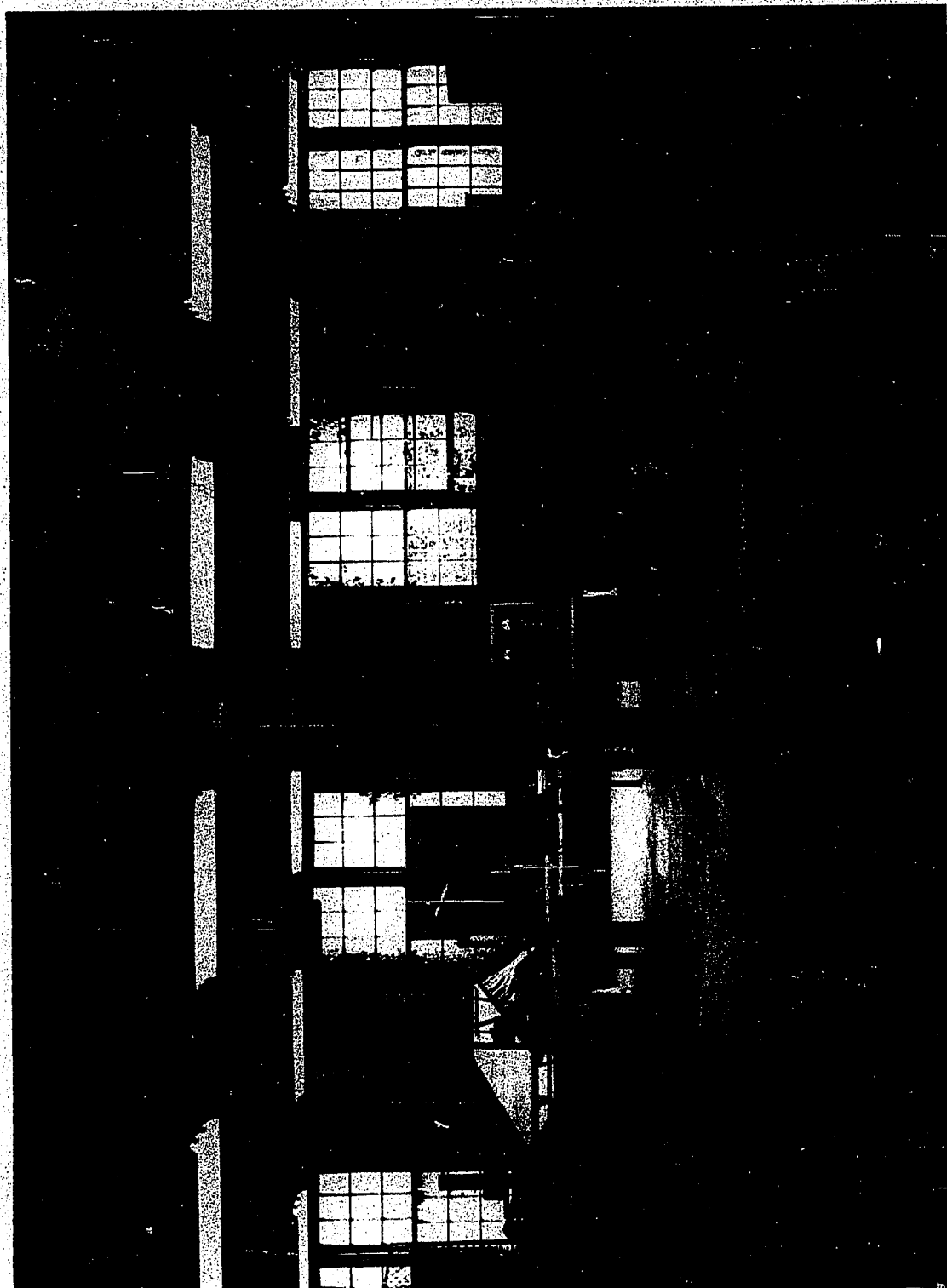
the actual velocity. If velocity profiles near the stagnation point are desired, the whole potential-flow solution will have to be iterated until sufficient accuracy results.

EXPERIMENTAL ANALYSIS

A picture of the test set-up is shown in Figure 6. The air source was a General Electric model 5GDY34C1 axial flow fan with a rated capacity of 3300 cfm at 2400 RPM with a static head of 3.25 in. of water. This fan is permanently installed in the Mechanical Engineering Laboratory of Iowa State University. The fan discharged into a four by four by eight foot surge box. The maximum available static head was about eight inches of water when flow was completely restricted. At one end of the surge box a Rotherm Engineering Company fiberglass nozzle was installed to provide a smooth transition section. The nozzle, designed according to American Society of Mechanical Engineers power test code specifications, had a nominal inside diameter of eight inches. The nozzle was flanged to the main test section.

The main test section consisted of an acrylic plastic pipe with a blunt nosed model concentrically inserted. The plastic pipe was flanged to the fiberglass nozzle. Although the pipe had a nominal diameter of eight inches, there was approximately a 0.005 inch difference between the inside diameters of the pipe and the nozzle. A gap was left in the flanged area which was filled with spackling putty to provide a smooth and continuous transition. The plastic pipe was drilled and tapped at several locations along the top to

Figure 6. Picture of experimental apparatus



Please Note: Pages 46, 51 and 80 are not original copy. They tend to "CURL".
Filmed best possible way.

University Microfilms, Inc.

accommodate a portable probe mount. Holes were provided at six inch intervals up to the blunt nose. Starting at the blunt-nose location, holes were provided every inch up to a point three inches behind the elliptical section. In the straight section behind, holes were provided every two inches along the remainder of the pipe. Socket head cap screws with rubber gaskets were used to plug the holes when not in use. The cap screws were filed and polished to match the interior surface. Although the screws had a 0.250 inch nominal diameter, the holes were drilled $1/32$ over to provide a slip fit for probes with a 0.250 inch shank.

The blunt-nose model was made in two sections which were held together with a threaded connector (see Appendix C). The elliptical section was machined from aluminum. The bottom was removable to facilitate servicing static pressure taps located along the top surface. The elliptical nose had a nominal six inch minor diameter and twelve inch major diameter with the major diameter in the axial direction.

The blunt nose was coupled to an eighteen inch long cylindrical section. The cylindrical section was made from a five and one half inch nominal outside diameter aluminum tube with a split acrylic plastic tube with one-quarter inch wall thickness surrounding it. The actual diameter of the completed model was 5.590 inches instead of the nominal six inches.

The blunt nose and the cylindrical section were roughed to shape separately and then finish machined and polished as a unit. Static pressure taps were provided on the model in the following manner. A 1/32 inch hole was drilled in the outside surface at an angle perpendicular to the tangent to the surface at that point. The holes were counter bored from the inside and quarter inch copper nipples were glued in the counterbored holes with an epoxy resin glue. Dean (20) in his discussion of static pressure taps indicated that the maximum error in static pressure measurement is of the order of 0.4% of the dynamic head when the tap hole is perpendicular to surface. One-quarter inch Dynalon pressure hoses were glued to the copper nipples and the hoses were led out the back of the model. Two additional taps were located 120° from the top center at a distance five inches behind the stagnation point. These taps assisted in ensuring concentric alignment of the model by balancing static pressures.

The blunt-nose model was supported in the plastic pipe by a bar behind the tube and four set screws located just behind the joining of the cylindrical section and the elliptical nose. Two set screws were located 45° away from the top centerline and the other two were located 120° away.

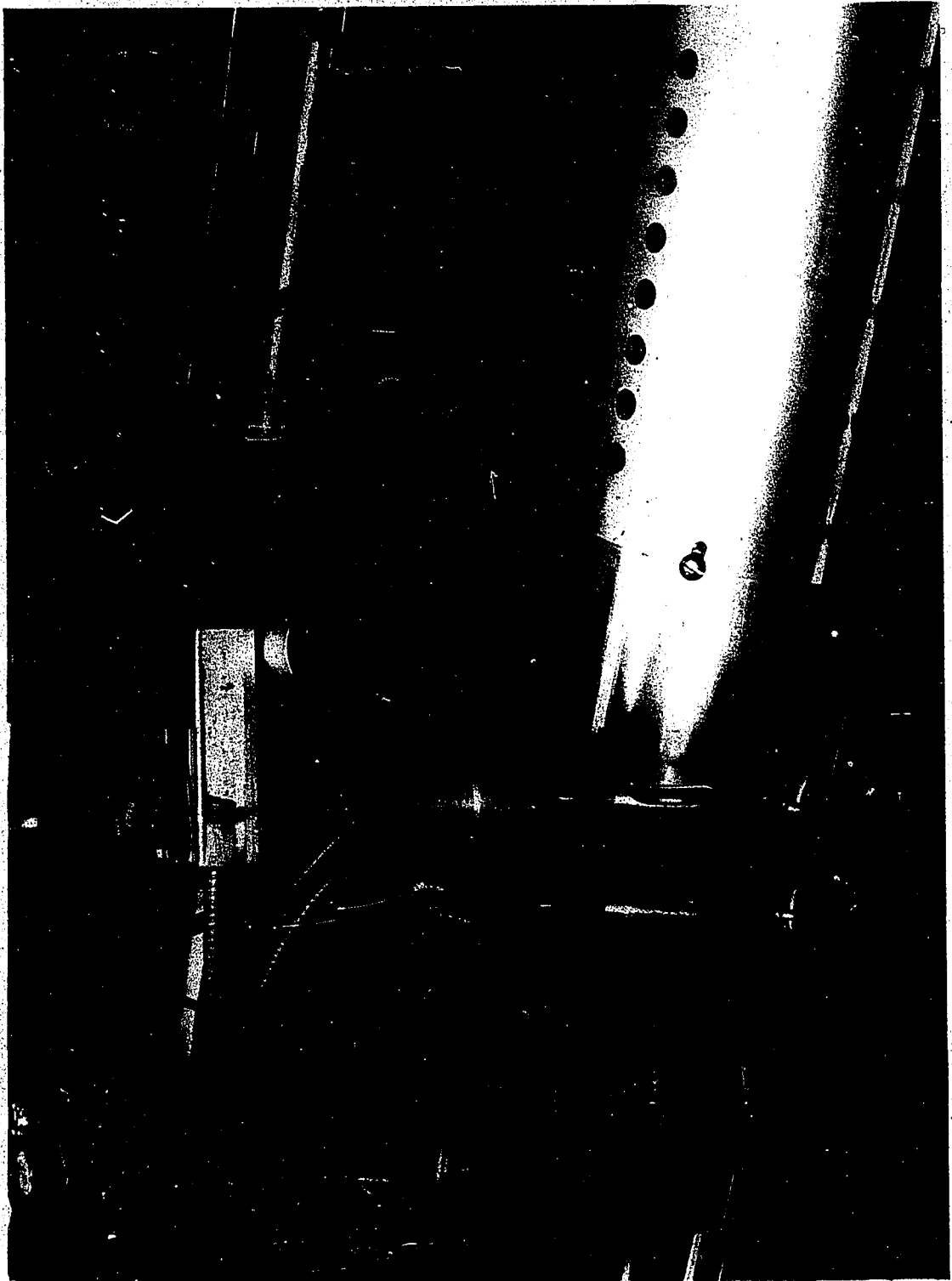
The portable probe mount was machined from mild steel and was supported by springs hooked to turnbuckles. The

probe holes in the plastic pipe were counter sunk $3/16$ inch and were one-half inch in diameter. The counter sunk hole was filled with a rubber gasket and vacuum grease to stop leakage. The rubber gasket was drilled to accommodate the shank of a pressure probe with a slip fit. The probe mount itself also was counterbored and this hole filled with vacuum grease and a drilled gasket. A rubber gasket was placed between the mount and the plastic pipe. No air leaks due to the probe mount and the probe hole were apparent.

An L. C. Smith model ABI-3 probe actuator was used to position the probe. (See Figure 7 for a close-up picture of the actuator and probe mount.) Although the actuator is calibrated to read in increments of $10/1000$ inch, it was possible to calibrate the revolutions of the gear driving the indicator dial to increments of $1.25/1000$ inch. It appeared that there was no backlash in the gearing system. As a precaution after the probe was initially positioned it was actuated in one direction only. After the data were taken for a given run the actuator was reversed and the measured data checked. The check proved reliable both as to probe and positioner.

Since the probe actuator also had an angular traverse it was a simple matter to rotate the probe until it faced directly into the flow by rotating the probe until the pressure was a maximum.

Figure 7. Close-up of probe actuator and probe mount



A Merriam model 34FB2 micromanometer accurate to 1/1000 inch of water was used as the primary measuring device. The Aerospace Engineering Department fifty tube manometer board was used for supplemental information to indicate that static pressure taps were functioning properly. The manometer board was inclined until one scale division on it corresponded to one scale division on a six inch inclined manometer. A Merriam model 40HE35 six inch inclined manometer was used to measure the static pressure in the surge box. It was accurate to 1/50 inch of water and was calibrated against the micromanometer. A model 40GE4 four-inch Merriam inclined manometer was used for supplemental measurement.

The dynamic head was measured with the micromanometer. A total-head probe was hooked to the high-pressure side of the micromanometer and the inside-wall static tap directly beneath the radial path of traverse of the total-head probe was connected to the low-pressure side. All dynamic heads were measured relative to the inner wall. At a given section the static pressure at the inside and outside surfaces were determined as functions of the surge-box pressure. A linear least-squares curve was fitted to the data.

Air temperature was measured with a mercury-in-glass thermometer accurate to 1/5 degree Fahrenheit. The static pressure, corrected for atmospheric pressure, and the

temperature were used to determine the fluid density using the perfect gas law. The fluid viscosity was determined using the temperature measured in the rear of the tube and applying it to the viscosity data of McAdams (32).

All pressure hose connections were securely wired and smothered with vacuum grease to prevent leakage. A soap solution was used to check for leaks.

Since incompressible flow was assumed, velocities were calculated from pressure measurements using the Bernoulli equation. The flow rate through the passage was determined by integrating the measured velocity profiles. The trapezoidal rule was applied to the differential expression $2\pi r u dr$. The total flow thus determined was divided by the area to determine the average velocity.

The method of error analysis suggested by Kline and McClintock (33) was used to estimate the error in velocity measurement. If this method is applied to the Bernoulli equation, the following form relates the error in calculated velocity to the error in measuring the differential pressure and density.

$$\frac{\sigma_U^2}{U^2} = \frac{\sigma_\rho^2}{4\rho^2} + \frac{\sigma_{\Delta p}^2}{4\Delta p^2},$$

where σ_U , σ_ρ , $\sigma_{\Delta p}$ are the errors in measuring the velocity, density and dynamic pressure respectively. The maximum

error in measuring the differential pressure was of the order of $3/1000$ inch allowing for pressure fluctuations. The maximum error in measuring the density was of the order of 0.0002 lb/ft^3 . Substituting these values in the above equation gave a maximum estimated error of 0.07 fps based on a velocity of 50 ft/sec or an error of 0.14% .

The primary probe used in this study was a United Sensor and Control, model BA-20, boundary-layer, total-head probe. The probe had a shank diameter of 0.020 inches. The head was flattened to a thickness of 0.010 inches. The surface angle of the elliptical nose made it impossible to use the probe as designed. Folsom (34) pointed out that probe geometry is relatively unimportant so long as the probe opening faced directly into the flow. The head of the probe was bent until it formed an angle parallel with the tangent to the wall. It was assumed that adjacent to the wall flow was approximately tangent to the wall and that the flow direction was the same as the tangent angle. The velocities so measured were assumed to be the true velocities at the centerline of the probe opening, neglecting disturbances produced by the probe itself. Outside the boundary layer the probe was calibrated against a United Sensor and Control probe, model DA-120, which had been factory calibrated.

When measuring the outer-wall boundary layer, the probe

head was bent slightly upward to ensure close contact with the outer wall. The probe used in this position was also calibrated against the DA-120 probe.

When working with probes with small openings a definite response time is evident. A Naval Ordnance Report dealing with wind-tunnel instrumentation (35) suggests that the response time of the probe be determined before actual measurements are taken. The response time of the boundary-layer probe was of the order of two minutes. It may have been less, but due to time necessary to adjust the micro-manometer, a minimum of two minutes was set as the standard before attempting a measurement. The inside- and outside-wall taps gave almost instantaneous response. There were pressure fluctuations in the passage of the order of 6/1000 inch of water. In making a measurement the upper and lower limits of the fluctuation were determined and the true pressure was assumed to be an average of the two.

The probe was positioned next to the wall by the reflection method. With a strong background light the probe was moved until it and its reflection met. It was possible to achieve almost this exact position whenever desired. In fact the initial position was checked at the end of each run and the relative pressures usually agreed.

When starting to traverse a profile, initial measurements were taken at 1.25/1000 inch intervals. The

velocities corresponding to the measured pressure were calculated whenever a measurement was made and the results were immediately plotted. This enabled the investigator to define the straight-line portion of the curve rather accurately and allowed him to lengthen out the intervals when the velocity gradient tapered off.

RESULTS AND DISCUSSION

Complete velocity profiles were determined at each of three locations in the inlet configuration shown in Appendix C and at each of three different Reynolds numbers at each location. The locations used corresponded to $z = 6$ inches, or the joining of the elliptical and cylindrical sections and the locations, $z = 4$ inches and $z = 2$ inches, further up the elliptical nose toward the stagnation point. At each location three velocity profiles corresponding to $N_{eq} = 43,700$, $61,500$, and $87,700$ were determined. It was observed that at a given position total and static pressure were linear functions of surge-box pressure. Therefore, all profiles at the same Reynolds number were corrected to a standard value of surge-box pressure by multiplying velocities by the square root of the ratio of the standard surge-box pressure to that measured during a given run.

At each section outside-wall and inner-wall static pressures were determined as functions of surge-box pressure. A linear least-squares curve was fitted to these data in order to determine the static pressure corresponding to the inside and outside wall taps. It was assumed that the static pressure varied linearly across a given section. Since all pressure differentials were measured relative to the inside-wall static tap, it was necessary to correct

velocities outside the inner-wall boundary layer by using the linear static pressure gradient assumption.

Knudsen and Katz (23) pointed out that in a velocity gradient the measured velocity is actually somewhat above the geometric center of the probe opening. They noted that the corrected curve of boundary-layer velocity versus distance from the wall, taking into account this variation, was similar to the measured curve, the only difference being that the corrected curve was shifted horizontally. Based on this observation Knudsen and Katz suggested that the slope of the theoretical curve be drawn through the origin and the measured data shifted until the straight-line portions of each curve coincided. This procedure was followed in all cases. The correction was of the order of 0.005 inches.

The corrected profiles were integrated to determine the momentum thickness. Up to the first data point, the actual value of the integral was obtained, assuming the portion of the curve up to this point was a straight line passing through the origin. From the first data point to the last, the trapezoidal rule was employed. The boundary-layer thickness was determined by multiplying the freestream velocity by 0.99 and determining the distance from the wall corresponding to this velocity. For purposes of calculation it was assumed that the measured velocity 0.10 inches away from either wall constituted the freestream velocity. (This

value, although arbitrarily chosen, was approximately twice the theoretical boundary-layer thickness.)

The results of the calculations of experimental inner-wall momentum thickness versus axial position at various Reynolds numbers are shown in Figure 8. The theoretical curves represent the momentum thickness distribution calculated from potential-flow solution. It will be noted that all of the data points lie consistently above the theoretical curve. This may be due in part to the difficulty of experimentally determining the boundary-layer thickness. A second iteration was performed using the approximate velocity distribution for a Reynolds number of 61,500. The resulting iteration produced results that were approximately 5% lower than the first iteration. The results of this iteration are shown in Figure 9 along with the curve calculated using the potential flow solution. A third iteration was not attempted since the boundary-layer thicknesses calculated from the second iteration differed from those calculated from the first iteration by only about 3%.

The curves assume their characteristic shape because of the acceleration distribution. Accelerations, $d\bar{U}/d\bar{x}$, calculated from the potential-flow solution are continually decreasing from the stagnation point. The approximate velocity distribution is merely an area ratio. Accelerations calculated from this distribution increase rapidly,

level off and then decrease toward the rear of the nose. The point where the curves of Figure 9 cross over occurs slightly behind the point of equal accelerations.

The boundary-layer parameters on the outer wall were checked against a theoretical solution by experimentally determining the constant of integration in Equation 3. This constant of integration turned out to be essentially zero indicating an extremely thin boundary layer opposite the stagnation point. This fact was confirmed by the inability of the author to make reliable measurements of the outer-wall boundary layer at the position $z = 2$ inches. At this station it was impossible to define the initial straight-line portion of the experimental curve and, therefore, no attempt was made to calculate the experimental momentum-thickness distribution. With a constant of integration of zero, the momentum-thickness distribution is within 3% of the momentum-thickness distribution on the inside wall. The experimental outer-wall momentum thicknesses are also shown in Figure 8. The actual outer-wall velocity profiles are plotted against the theoretical curves obtained from the inner-wall momentum-thickness distribution.

The boundary-layer data were plotted against the theoretical curves determined from the potential-flow solution. The boundary-layer thickness was calculated from the momentum thickness using the methods of Appendix A. The

actual potential velocity on the inner and outer wall, assuming the potential velocity at $z = 6$ inches was equal to U_{avg} , was used in the boundary-layer profile equation, Equation 2A. The results are shown in Figures 10, 11, and 12. The interior velocities are shown in Figures 13 and 14 with the theoretical curve calculated from the potential-flow solution. It should be noted that the approximate solution would indicate a uniform velocity distribution over the interior region. Near the forward portion of the nose the distribution is definitely skewed, being larger at the inside wall than at the outside. For the section $z = 6$ inches, interior velocities were uniform across the passage.

The boundary layer profiles for the inside wall, $z = 6$ inches, $N_{eq} = 61,500$, using the potential-flow solution and the approximate solution, first and second iterations, are shown in Figure 15. Even though momentum-thickness distributions may differ, this difference is not as pronounced when calculating the boundary-layer thickness since the acceleration is used in determining this thickness. The ratio of momentum thickness to acceleration, $d\bar{U}/d\bar{x}$, turned out to be approximately constant for all three curves at a given section.

Average velocities, U_{avg} , were determined by integrating the velocity profile across the section corresponding to $z = 6$ inches and dividing by the passage area. Weight flows

were checked for $N_{eq} = 61,500$ at sections $z = 4$ inches and $z = 2$ inches by integration and deviated from the weight flow determined for $z = 6$ inches by less than one per cent. At the two forward sections where the flow was not completely axial, it was assumed that the flow angle varied linearly across the passage and varied from a value equal to the angle of the tangent line to the inside surface to completely axial on the outside surface.

A summary of all experimental data is presented in Figure 16. Velocities are plotted using the dimensionless ratio U/U_{max} , where U_{max} is the maximum measured velocity at a given section and at a given Reynolds number. These profiles resemble very closely the data of Sega and Yokoyama (18). Their data were presented in figures that were too small to be of use for quantitative comparison.

Figure 8. Theoretical and measured momentum-thickness distribution for various Reynolds numbers

(Theoretical distribution calculated from the potential-flow solution)

Momentum
thickness,
inches

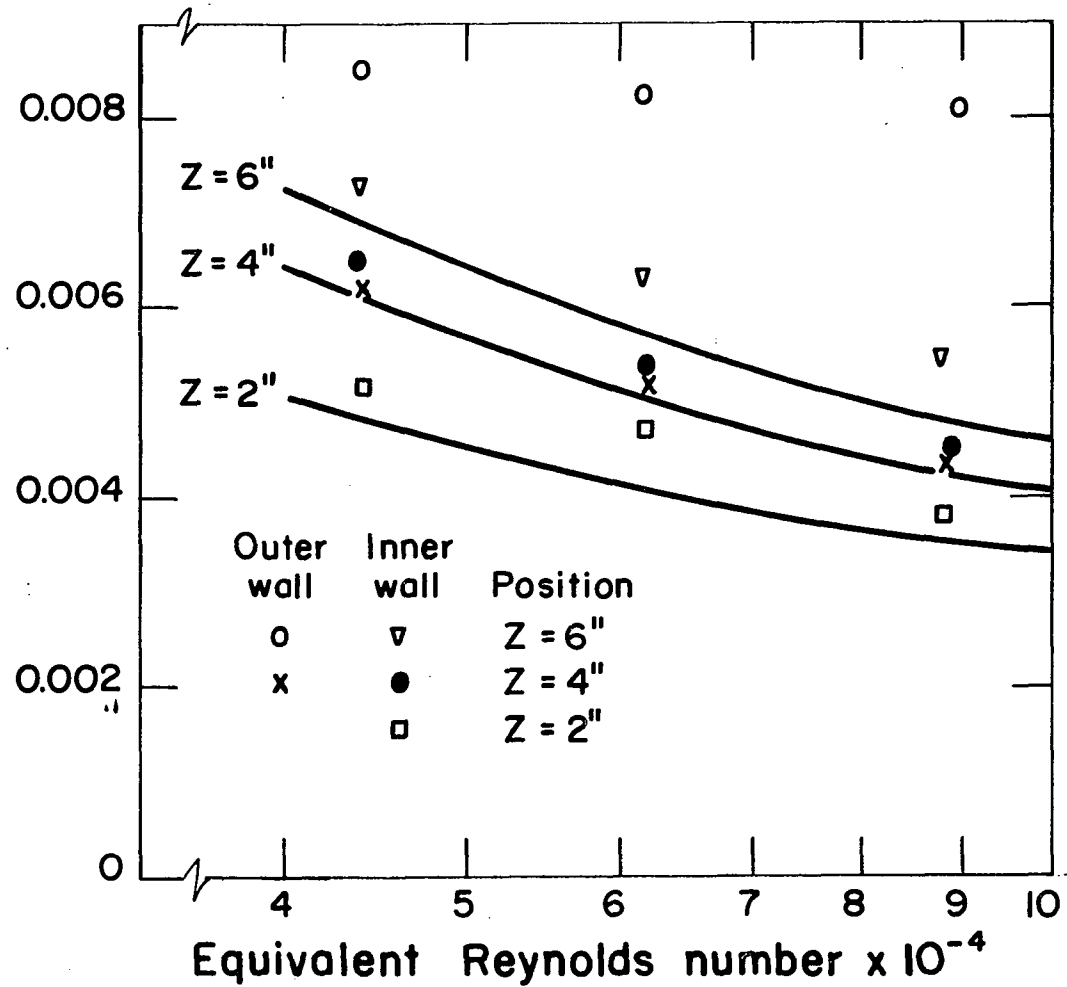


Figure 9. Theoretical and measured momentum-thickness distribution for
 $N_{eq} = 61,500$

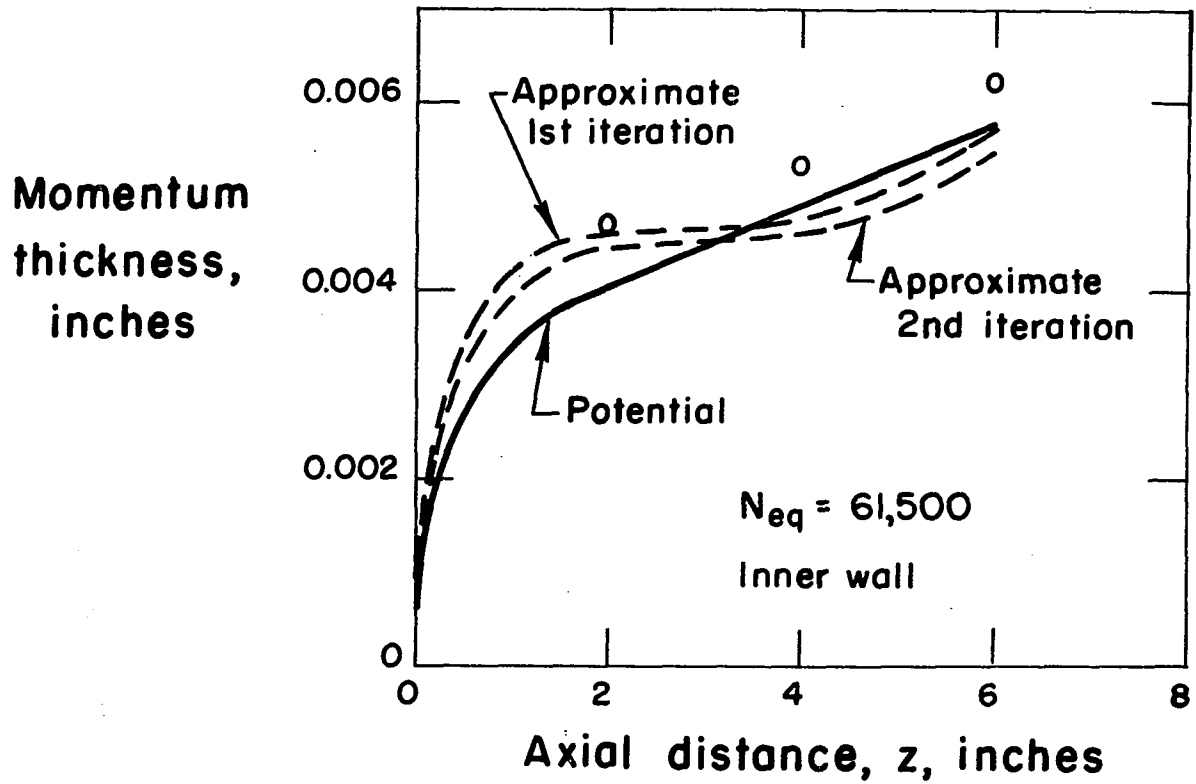


Figure 10. Inner- and outer-wall boundary-layer velocities for $z = 6$ inches
(Theoretical curve calculated from potential-flow solution)

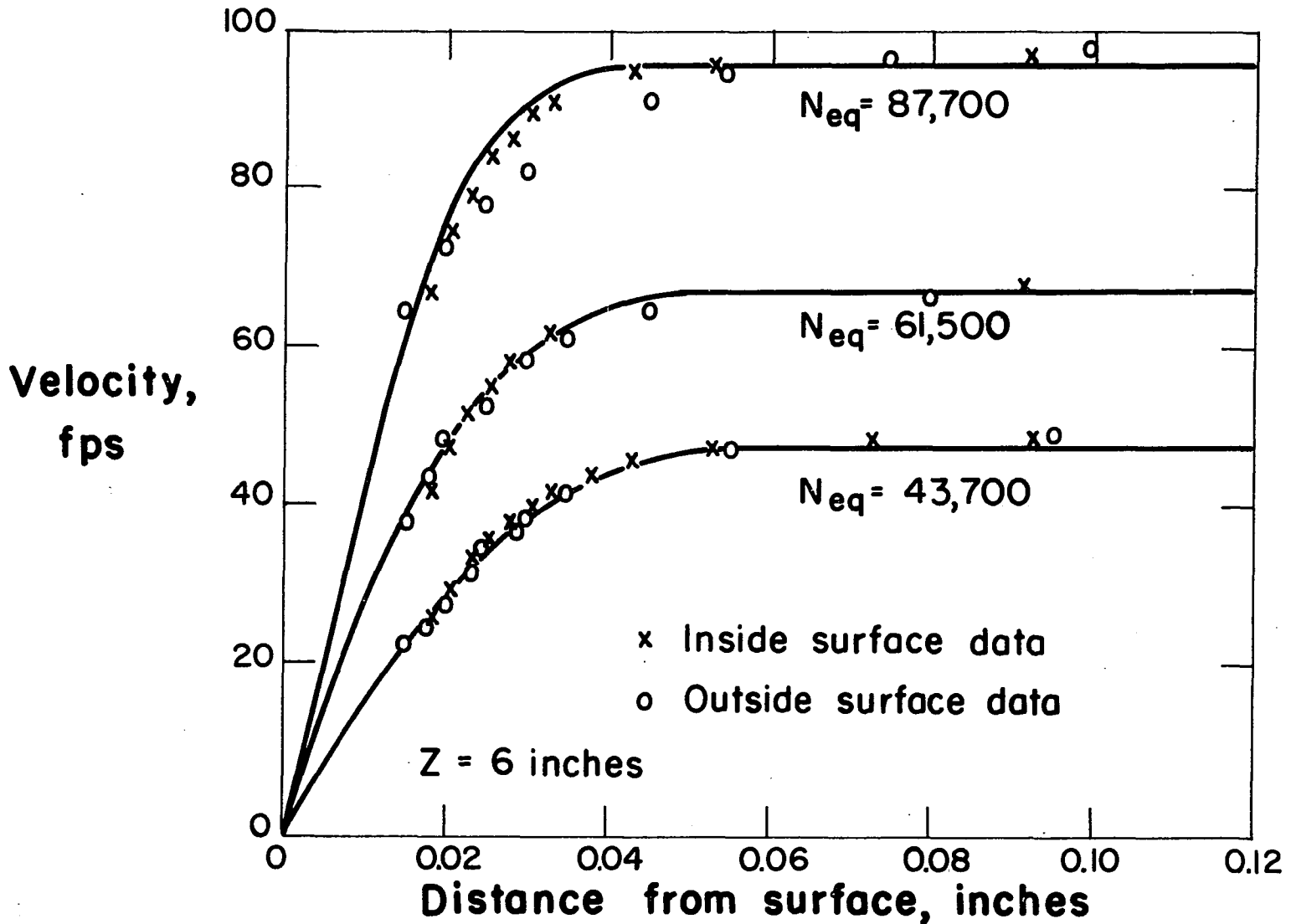


Figure 11. Inner- and outer-wall boundary-layer velocities for $z = 4$ inches
(Theoretical curve calculated from potential-flow solution)

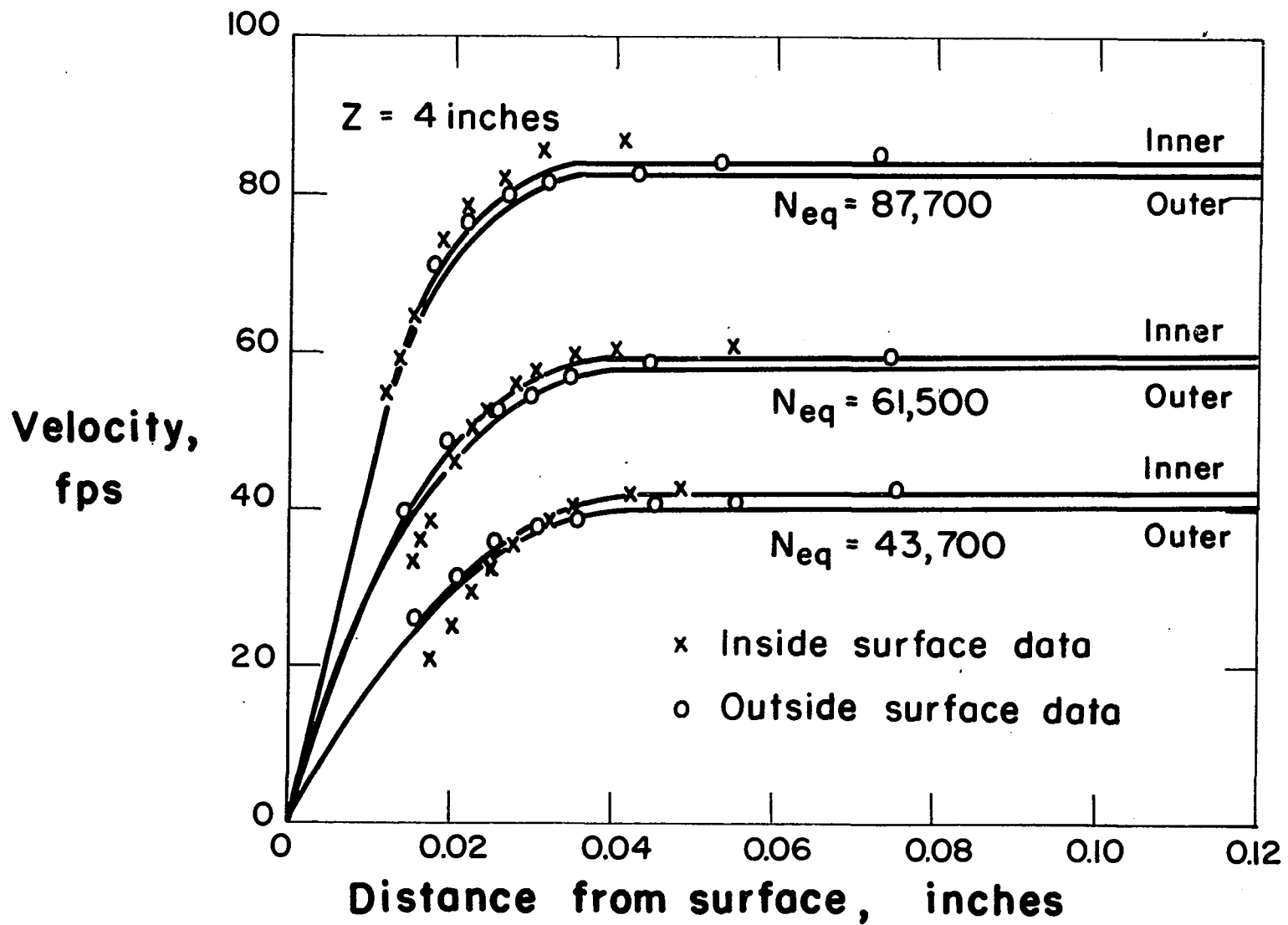


Figure 12. Inner- and outer-wall boundary-layer velocities for $z = 2$ inches
(Theoretical curve calculated from potential-flow solution)

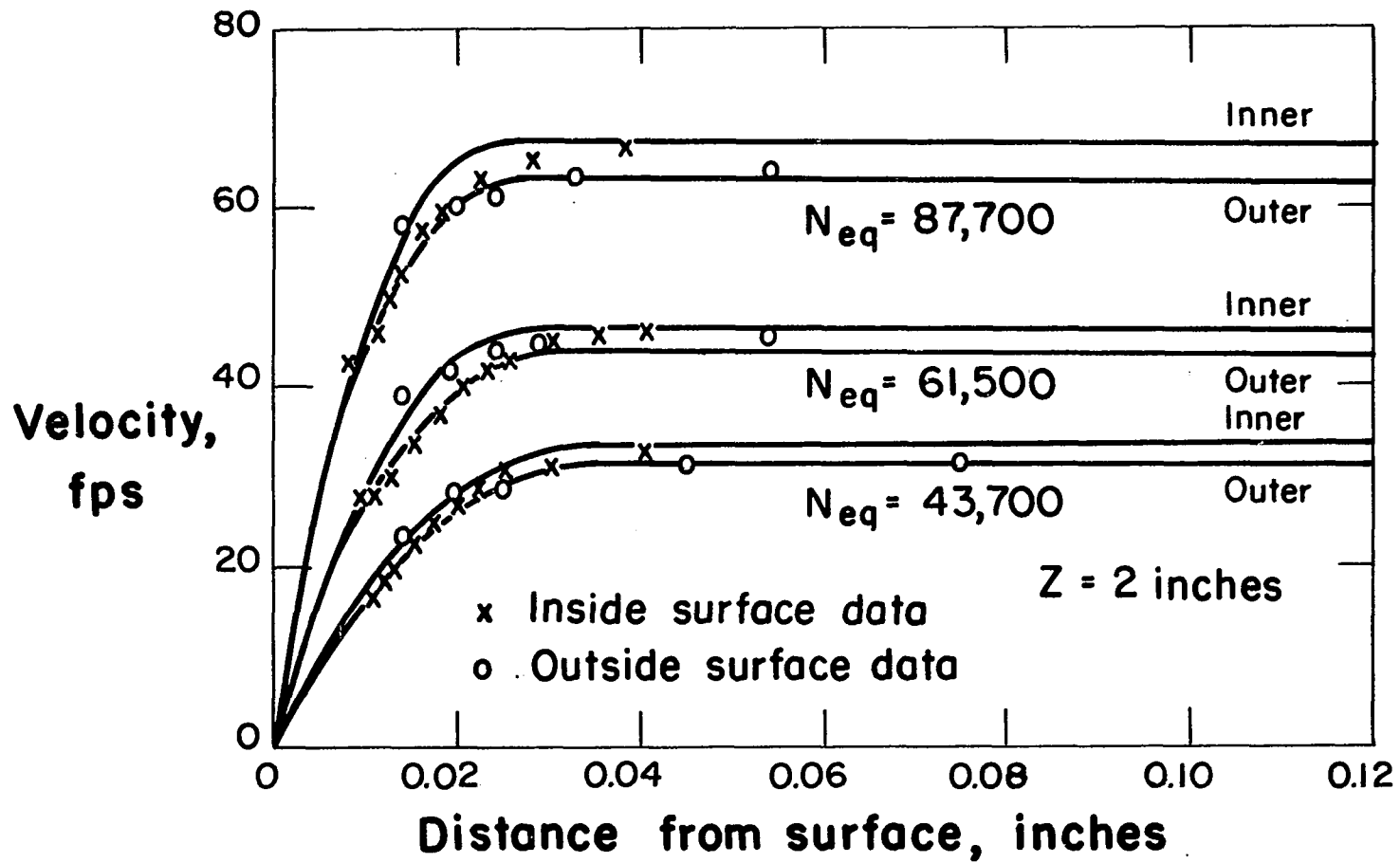


Figure 13. Potential core velocity distribution for $z = 4$ inches
(Theoretical curve calculated from potential-flow solution)

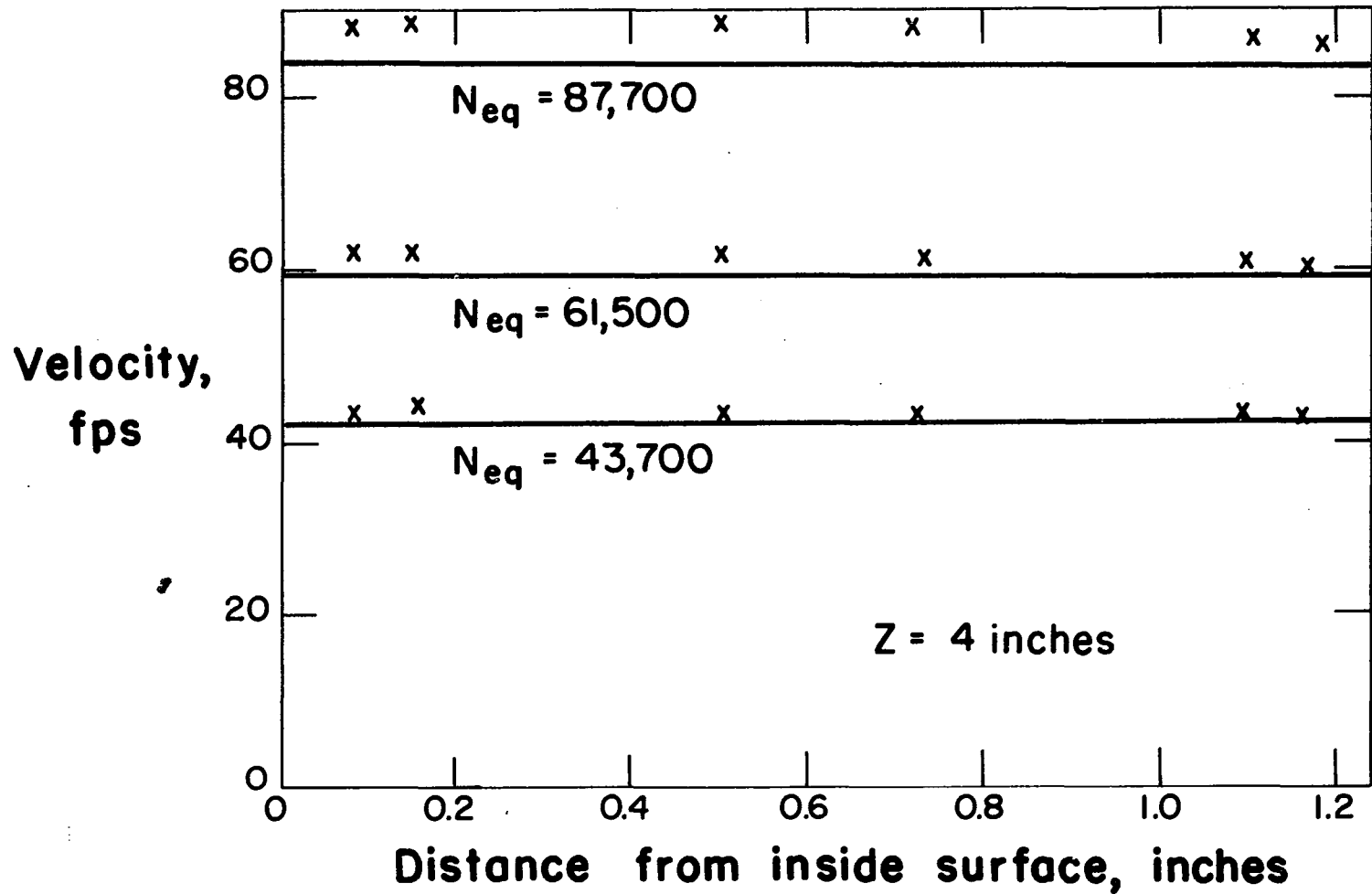


Figure 14. Potential core velocity distribution for $z = 2$ inches
(Theoretical curve calculated from potential-flow solution)

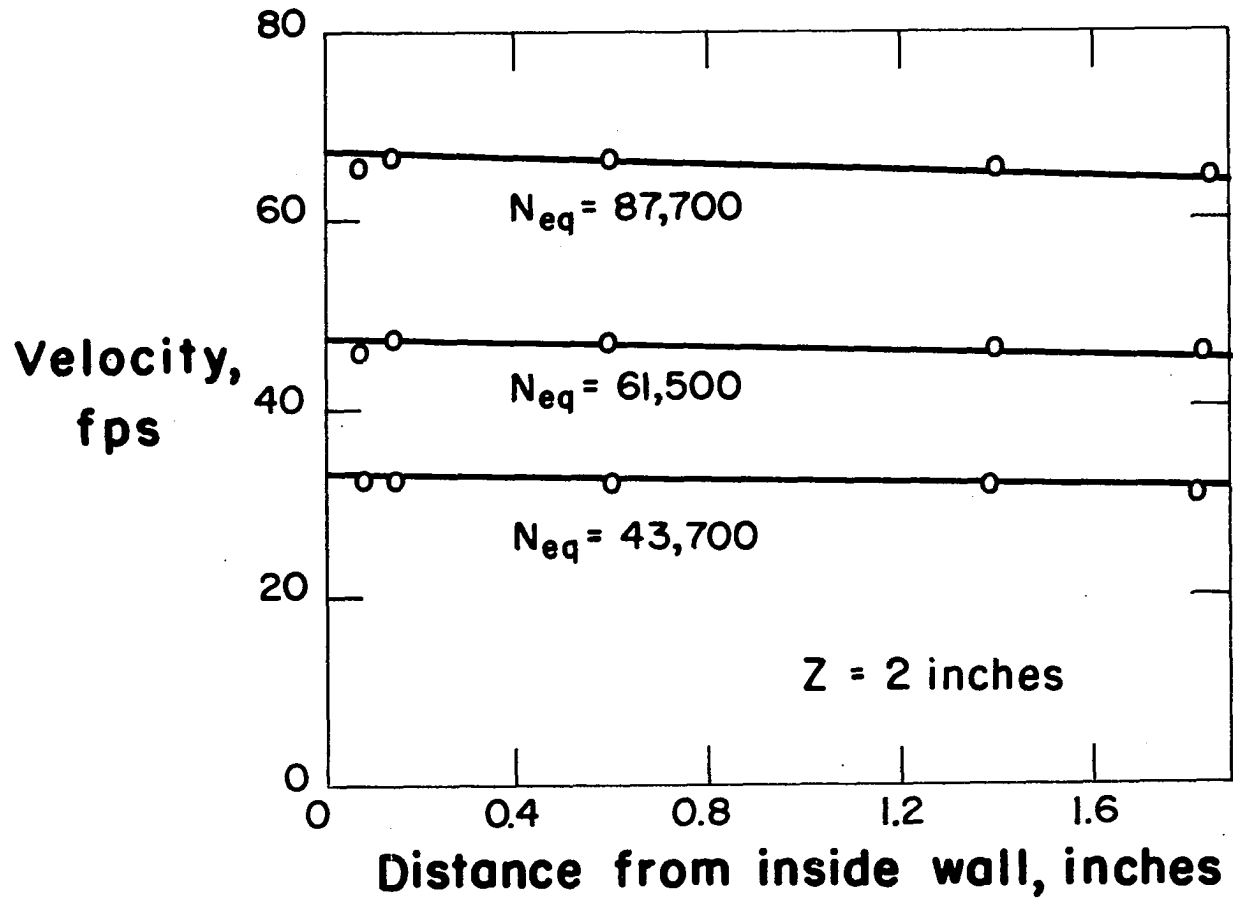


Figure 15. Inner-wall boundary-layer velocities for $z = 6$ inches and $N_{eq} = 61,500$ showing effect of potential core velocity assumptions

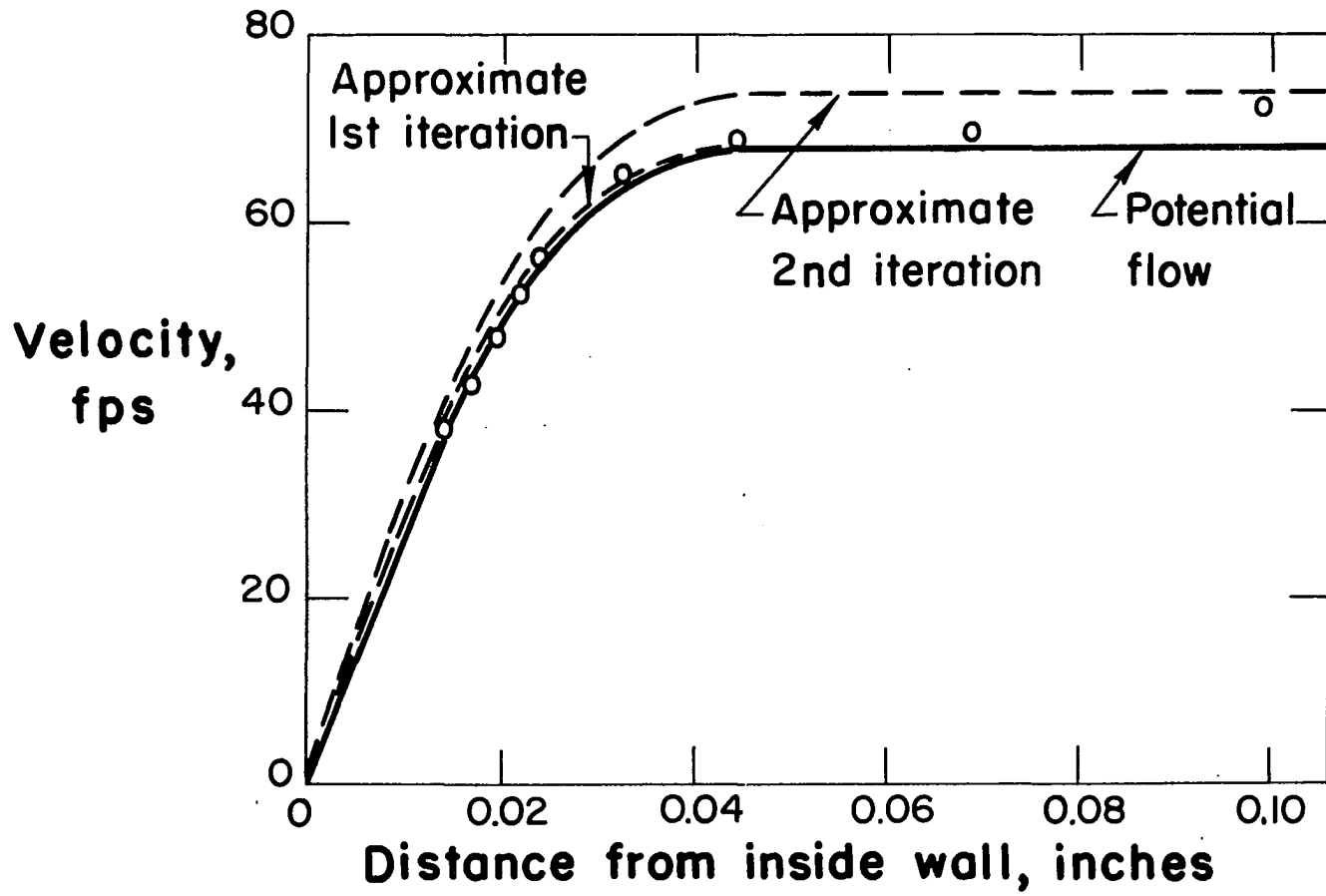
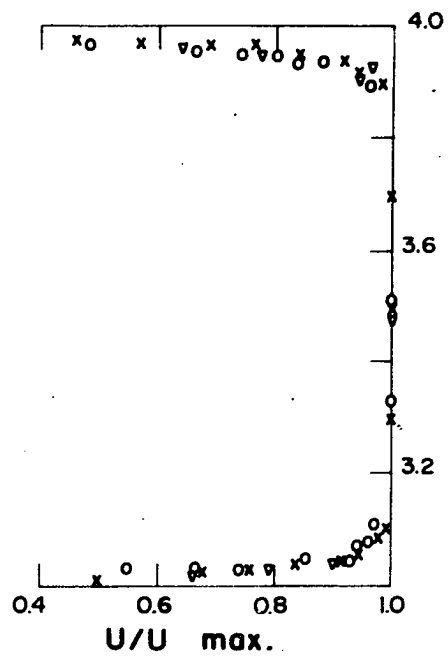
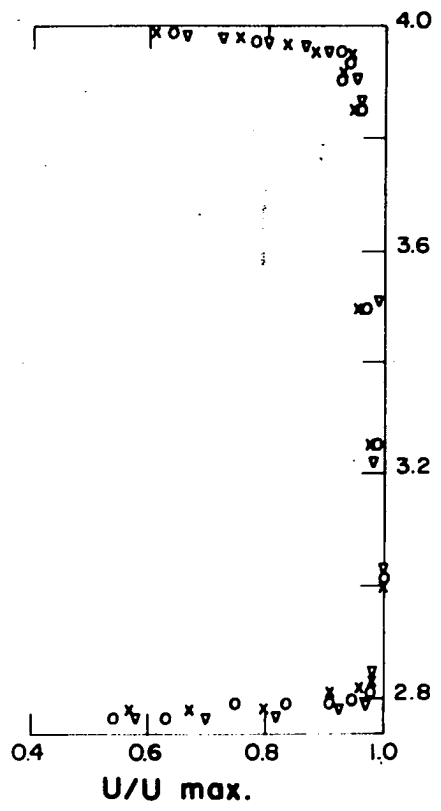
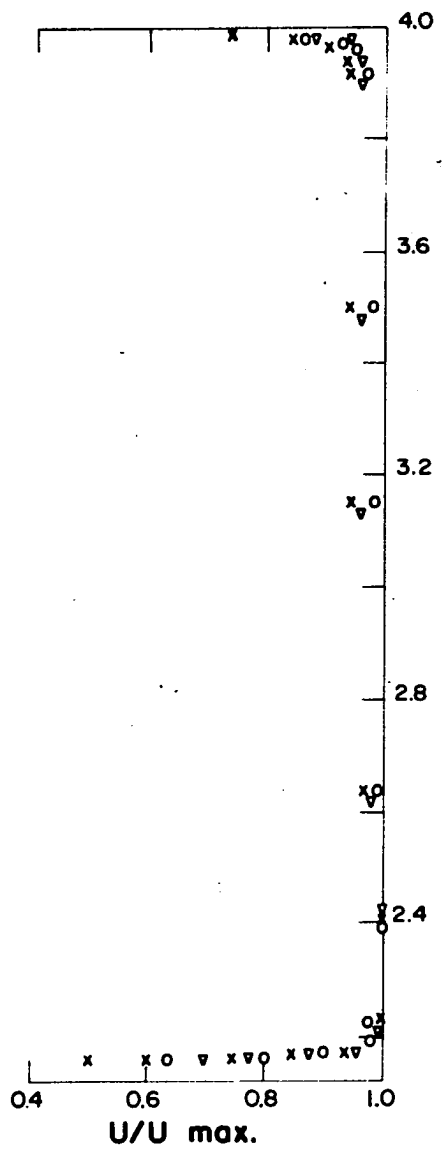


Figure 16. Summary of all measured velocity profiles



- x $N_{eq} = 43,700$
- o $N_{eq} = 61,500$
- v $N_{eq} = 87,700$

All ordinates represent distance from centerline in inches.

CONCLUSIONS

The proposed method for evaluating boundary-layer parameters gave reliable results. This would justify the assumptions regarding its formulation. Of particular interest is the fact that the method for determining the constant of integration in Equation 3, i.e., assuming the body of revolution is spherical in the neighborhood of the stagnation point, appears to be justified. All boundary-layer velocity profiles appeared to be laminar even though flow through the upstream section of pipe was at Reynolds numbers indicative of turbulent flow.

The approximate velocity distribution gave results which compared favorably with the results calculated from the more accurate potential flow solution. This fact greatly simplifies application of the method.

The outer-wall boundary layer still requires more study. Because the eight foot length of pipe leading up to the annular passage is not typical of engineering applications, further study should be focused on the outer-wall effects produced by placing the body of revolution directly in the bell-mouth.

Effects of rotation encountered in actual machines were not considered in this study. The relative velocity component induced by an actual rotor could have definite

effects on the theoretical boundary-layer velocity profiles, even though the experimental evidence produced in this study conformed generally to data taken from actual machines.

Toward the forward stagnation point, velocities were a maximum at the inside surface, tapering off by about 10% at the outside wall. An examination of potential flow solution reveals that toward the stagnation point inside-surface accelerations are higher than outside-surface accelerations. It is suggested that inlet sections with more pronounced curvature on the inside wall would exhibit higher inside-wall velocities relative to the outside wall. In a realistic inlet situation with a bladed rotor and with supporting struts, this effect could be even more pronounced. For example, a constant-area strut restricts flow more toward the inside wall than it does on the outside, thereby increasing inner-wall velocities.

Finally, it should be mentioned that this study dealt with only one configuration. Additional work on different nose configurations, and on different inside- to outside-wall diameter ratios should be undertaken before the method is completely justified.

LITERATURE CITED

1. Andrews, S. J., Jeffs, R. A., and Hartley, E. L. Tests concerning novel designs of blades for axial compressors. Great Britain Aero. Res. Council. Rep. and Memo. 2929. 1951.
2. Serovy, G. K. and Anderson, E. W. Method for predicting off-design performance of axial-flow compressor blade rows. U.S. Nat. Aero. and Space Admin. Tech. note D-110. 1959.
3. Carter, A. D. S. Three dimensional-flow theories for axial compressors and turbines. Inst. Mech. Engr. Proc. 159: 255-268. 1948.
4. Hatch, J. E. and Bernatowicz, D. T. Aerodynamic design and performance of first spool of a 24-inch two-spool transonic compressor. U.S. Nat. Adv. Comm. Aero. Res. Memo. E56L07a. 1957.
5. Serovy, G. K. and Lysen, J. C. Prediction of axial-flow turbomachine performance by blade-element methods. Amer. Soc. of Mech. Engr. Paper 61-WA-134. New York, N.Y., The Society. 1961.
6. Vavra, M. H. Steady flow of nonviscous elastic fluids in axially symmetric channels. Jour. Aero. Sci. 17: 149-157. 1950.
7. Ellis, G. O., Stanitz, J. D., and Sheldrake, L. J. Two axial-symmetry solutions for incompressible flow through a centrifugal compressor with and without inducer vanes. U.S. Nat. Adv. Comm. Aero. Tech. Note 2464. 1951.
8. Spannhake, Wilhelm. Centrifugal pumps, turbines, and propellers. Cambridge, Mass., The Technology Press, Massachusetts Institute of Technology. 1934.
9. Gibbings, J. C. The design of an annular entry to a circular duct. Aero. Quarterly 10: 361-372. 1959.
10. Horlock, J. H. and Lewis, R. I. Shear flow in straight-sided nozzles and diffusers. Intl. Jour. Mech. Sci. 2: 251-266. 1961.

11. Woods, L. C. Compressible subsonic flow in two-dimensional channels, Part II: The application of the theory to problems of channel flow. *Aero. Quarterly* 6: 254-276. 1955.
12. Carrier, G. F. Elbows for accelerated flow. *Amer. Soc. Mech. Engr. Jour. Appl. Mech. Trans.* 14: 108-112. 1947.
13. Abdurahiman, P. V. Two-dimensional compressible flow past a solid body symmetrically placed in a channel. *Great Britain Aero. Res. Council. Rep. and Memo.* 1678. 1947.
14. Emmons, H. W. Flow of a compressible fluid past a symmetrical airfoil in a wind tunnel and in free air. *U.S. Nat. Adv. Comm. Aero. Tech. Note* 1746. 1948.
15. Sacks, A. H. and Spreiter, J. R. Theoretical investigation of submerged inlets at low speeds. *U.S. Nat. Adv. Comm. Aero. Tech. Note* 2323. 1951.
16. Ruden, P. Two-dimensional symmetric inlets with external compression. *U.S. Nat. Adv. Comm. Aero. Tech. Memo.* 1279. 1950.
17. Nichols, M. R. and Rinkoski, D. W. A low-speed investigation of an annular transonic air inlet. *U.S. Nat. Adv. Comm. Aero. Tech. Note* 2685. 1952.
18. Sega, M. and Yokoyama, E. Experimental investigation of axial-compressor inlets. *Japan Soc. Mech. Engr. Bulletin* 2: 451-457. 1959.
19. Johnston, I. H. The effect of inlet conditions on the flow in annular diffusers. *Great Britain Aero. Res. Council. Current Paper* 178. 1954.
20. Dean, R. C., Jr. *Aerodynamic measurements.* Cambridge, Mass., Gas Turbine Laboratory, Massachusetts Institute of Technology. 1953.
21. Schlichting, Dr. Hermann. *Boundary layer theory.* New York, N.Y., McGraw-Hill Book Company, Inc. 1958.
22. Rott, N. and Crabtree, L. F. Simplified laminar boundary-layer calculations for bodies of revolution and for yawed wings. *Jour. Aero. Sci.* 19: 553-565. 1952.

23. Knudsen, James G. and Katz, Donald L. Fluid dynamics and heat transfer. New York, N.Y., McGraw-Hill Book Company, Inc. 1958.
24. Thwaites, B. Approximate calculation of the laminar boundary layer. Aero. Quarterly 1: 245-280. 1949.
25. Truckenbrodt, E. Ein Quadraturverfahren sur Berechnung der laminaren und turbulenten Reibungsschicht bei ebener und rotationssymmetrischer Stromung. Ing.-Arch. 20: 211-228. 1952.
26. Loitsianskii, L. G. Approximate method of integration of laminar boundary layer in incompressible fluid. U.S. Nat. Adv. Comm. Aero. Tech. Memo. 1293. 1951.
27. Wright, E. A. and Bailey, G. W. Laminar frictional resistance with pressure gradient. Jour. Aero. Sci. 164: 547-579. 1938.
28. Millikan, C. B. The boundary layer and skin friction for a figure of revolution. Amer. Soc. Mech. Engr. Trans. 54: 29-39. 1932.
29. Bussmann, K. and Ulrich, A. Systematic investigations of the shape of the profile upon the position of the transition point. U.S. Nat. Adv. Comm. Aero. Tech. Memo. 1185. 1947.
30. Rivas, M. A. and Shapiro, A. On the theory of discharge coefficients for rounded-entrance flow meters. Amer. Soc. Mech. Engr. Trans. 78: 489-497. 1956.
31. Prandtl, L. and Tietjens, O. G. Applied hydro- and aeromechanics. New York, N.Y., Dover Publications, Inc. 1957.
32. McAdams, William H. Heat transmission. New York, N.Y., McGraw-Hill Book Company, Inc. 1954.
33. Kline, S. J. and McClintock, F. A. Describing uncertainties in single sample experiments. Mechanical Engineering 75: 3-8. 1953.
34. Folsom, R. G. Review of the pitot tube. Amer. Soc. Mech. Eng. Trans. 78: 1447-1460. 1956.

35. Volluz, R. J. Wind tunnel instrumentation and operation. Handbook of supersonic aerodynamics. Vol. 6, Section 20. U.S. Bureau of Naval Weapons, NAVORD Report 1488, Vol. 6. 1961.
36. Salvadori, Mario G. and Baron, Melvin L. Numerical methods in engineering. Englewood Cliffs, N.J., Prentice-Hall, Inc. 1961.
37. Forsythe, George E. and Wasow, Wolfgang R. Finite-difference methods for partial differential equations. New York, N.Y., John Wiley and Sons, Inc. 1960.

ACKNOWLEDGMENTS

The author's graduate program was directed by a committee composed of Dr. E. W. Anderson, Professor H. M. Black, Professor R. C. Fellingner, Dr. C. T. Hsu, Dr. G. K. Serovy, and Dr. H. J. Weiss. The assistance and guidance offered by these men is greatly appreciated.

Dr. G. K. Serovy directed the preparation of this dissertation. Words cannot express the author's admiration for this man.

The assistance of the National Aeronautics and Space Administration was an integral part of this project. The suggestions offered by Mr. J. Crouse and Mr. M. Hartman of the Lewis Research Center, Cleveland, Ohio, were invaluable.

This project was launched through a grant from the President's Permanent Objective Committee of the Alumni Achievement Fund.

The Iowa Engineering Experiment Station under the direction of Dr. D. R. Boylan contributed substantially to the completion of this project.

APPENDIX A

Development of Laminar Boundary-Layer Equations
over a Body of Revolution

At the risk of being redundant, brief mention will be made of Pohlhausen's approximate method for the case of a pressure gradient in two-dimensional flow. This solution leads to a simplification in evaluating the shape parameter. Further it will be shown that the relations developed by Pohlhausen for two-dimensional flow can be transformed to apply to a body of revolution.

The discussion which follows, through Equation 12A, is based on Schlichting (21, pp. 206-219). Pohlhausen's original paper was not available to this author. In addition, since Pohlhausen's work has become a classic boundary-layer problem, this solution can be found in numerous textbooks.

The approximate method of Pohlhausen for laminar boundary layer with a pressure gradient assumes a velocity profile of the form

$$\frac{u}{U} = f(n) = an + bn^2 + cn^3 + dn^4, \quad n = \frac{y}{s} \quad (\text{Eq. 1A})$$

where y is the distance normal to the surface and s is the boundary-layer thickness. Observe that this profile implies

similarity in that u is not a function of x , but only of n . In order to evaluate the constants, four boundary conditions are necessary.

$$y = 0; \quad u = 0, \quad v \frac{\partial^2 u}{\partial y^2} = \frac{1}{\rho} \frac{dp}{dx} = U \frac{dU}{dx}$$

$$y = s; \quad u = U, \quad \frac{\partial u}{\partial y} = 0, \quad \frac{\partial^2 u}{\partial y^2} = 0$$

If we introduce a shape factor

$$S = \frac{s^2}{v} \frac{dU}{dx},$$

Equation 1A becomes

$$\frac{u}{U} = F(n) + S G(n) \quad (\text{Eq. 2A})$$

$$F(n) = 1 - (1 - n)^3 (1 + n)$$

$$G(n) = \frac{1}{6} n (1 - n)^2.$$

If this velocity profile, Equation 2A, is substituted in the definitions for displacement thickness and momentum thickness (see List of Symbols for these definitions), the following relations result.

$$\frac{s^*}{s} = \frac{3}{10} - \frac{S}{120} \quad (\text{Eq. 3A})$$

$$\frac{\theta}{s} = \frac{37}{315} - \frac{S}{945} - \frac{S^2}{9072} \quad (\text{Eq. 4A})$$

Thus it may be seen that the problem is mainly one of determining S , which is a function of x . In order to evaluate the function $S(x)$, consider first the momentum equation.

$$U^2 \frac{d\theta}{dx} + (2\theta + s^*) U \frac{dU}{dx} = \frac{t_o}{\rho} \quad (\text{Eq. 5A})$$

If Equation 5A is multiplied by $\theta/\nu U$, the following form results, where the prime denotes differentiation with respect to x .

$$\frac{U\theta\theta'}{\nu} + \left(2 + \frac{s^*}{\theta}\right) \frac{\theta^2 U'}{\nu} = \frac{t_o \theta}{\mu U} \quad (\text{Eq. 6A})$$

Schlichting (21) reports a simplification resulting from the work of Holstein and Bohlen who introduce a second shape factor, K , where

$$K = \frac{\theta^2}{\nu} \frac{dU}{dx} .$$

In addition, Schlichting defines a third shape factor, Z ,

where

$$Z = \frac{\theta^2}{v} \quad \text{or} \quad K = Z \frac{dU}{dx} .$$

If Equations 3A and 4A are substituted in Equation 6A,

$$K = \left(\frac{37}{315} - \frac{S}{945} - \frac{S^2}{9072} \right) S , \quad (\text{Eq. 7A})$$

$$\frac{s^*}{\theta} = \left(\frac{3}{10} - \frac{S}{120} \right) / \left(\frac{37}{315} - \frac{S}{945} - \frac{S^2}{9072} \right) = f_1(K) , \quad (\text{Eq. 8A})$$

$$\frac{t_o \theta}{U} = \left(2 + \frac{S}{6} \right) \left(\frac{37}{315} - \frac{S}{945} - \frac{S^2}{9072} \right) = f_2(K) . \quad (\text{Eq. 9A})$$

Equations 7A, 8A, and 9A are now substituted into the momentum Equation 6A.

$$\frac{1}{2} U \frac{dZ}{dx} + (2 + f_1(k))K = f_2(K) \quad (\text{Eq. 10A})$$

This equation, although complex, can be integrated because the functions $f_1(K)$ and $f_2(K)$ are universal functions and are independent of body shape. If a new parameter, $F(K)$, is defined,

$$F(K) = 2f_2(K) - 4K - 2Kf_1(K),$$

Equation 10A becomes,

$$\frac{dZ}{dx} = \frac{F(K)}{U}, \quad K = ZU' \quad . \quad (\text{Eq. 11A})$$

The functions $K(S)$, $f_1(K)$, $f_2(K)$ and $F(K)$ are tabulated in Schlichting (21), Table 12.2.

Schlichting pointed out a further simplification due to Waltz who observed that the function $F(K)$ could be quite closely approximated by a straight line.

$$F(K) = a - bK$$

with $a = 0.470$ and $b = 6$. Equation 11A now becomes, upon substituting this approximation,

$$U \frac{dZ}{dx} = a - bK \quad .$$

Substituting the definitions for Z and K

$$\frac{d}{dx} \left(\frac{U\theta^2}{\nu} \right) = a - (b - 1) \frac{U\theta^2}{\nu} \frac{1}{U} \frac{dU}{dx}$$

and upon integrating

$$\frac{U\theta^2}{\nu} = \frac{a}{U^{b-1}} \int_{x=0}^x U^{b-1} dx + C_1 \quad .$$

If the values for a and b are substituted, the final form results,

$$\frac{U\theta^2}{\nu} = \frac{0.470}{U^5} \int_{x=0}^x U^5 dx + C_1 . \quad (\text{Eq. 12A})$$

If the free stream velocity distribution, U, is known, Equation 12A may be integrated directly and $U\theta^2/\nu$ will be known as a function of x. If dU/dx is also known, K can be computed directly. Knowing K, it is possible to use the tables presented in Schlichting to calculate the first form factor, S. When S is known, the velocity profile is established at every value of x and the boundary layer thickness, s, and the displacement thickness, s^* , can be calculated.

The extension of the above methods to a body of revolution is a comparatively simple matter. In fact, the problem can be attacked in an entirely analagous manner. The momentum equation for the case of a body of revolution is

$$U^2 \frac{d\theta}{dx} + (2\theta + s^*) U \frac{dU}{dx} + U^2 \frac{\theta}{r} \frac{dr}{dx} = \frac{t_o}{\rho} . \quad (\text{Eq. 13A})$$

If Equation 13A is multiplied by $\theta/\nu U$ and the definitions substituted as before, assuming the Pohlhausen velocity distribution

$$\frac{1}{2} U \frac{dZ}{dx} = \frac{1}{U} (2 + f_1(K)) + \frac{1}{r} \frac{dr}{dx} \frac{U}{U'} K = f_2(K) . \quad (\text{Eq. 14A})$$

Introducing $F(K)$ as before

$$\frac{dZ}{dx} = \frac{1}{U} (F(K) - 2K \frac{1}{r} \frac{dr}{dx} \frac{U}{U'}) . \quad (\text{Eq. 15A})$$

Equation 15A differs from Equation 11A only by the second term in the bracket. Since $1/r \cdot dr/dx \cdot U/U'$ is known from the body shape and the potential-flow solution, Equation 15A can be solved.

Rott and Crabtree (22) use Equation 13A in the form

$$\frac{U^2}{r} \frac{d}{dx} (\theta r) + (2\theta + s^*) U \frac{dU}{dx} = \frac{t_o}{\rho} .$$

Again, multiplying through by $\theta/\nu U$

$$\frac{U^2 \theta}{\nu r} \frac{d}{dx} (\theta r) + (2 + \frac{s^*}{\theta}) \frac{\theta^2 U'}{\nu} = \frac{t_o \theta}{\mu U} ,$$

or in terms of the previous parameters

$$\frac{U \theta}{\nu r} \frac{d}{dx} (\theta r) + (2 + f_1(K)) K = f_2(K) ,$$

substituting the definition of $F(K)$, the final form becomes

$$\frac{U \theta}{\nu r} \frac{d}{dx} (\theta r) = \frac{1}{2} F(K) .$$

The following definitions may now be made.

$$R = \frac{\theta^2 r^2}{v}, \quad \frac{dR}{dx} = \frac{2\theta r}{v} \frac{d}{dx} (\theta r), \quad \frac{U}{r^2} \frac{dR}{dx} = F(K) \quad (\text{Eq. 16A})$$

If the assumption of Waltz is used

$$\frac{U}{vr^2} \frac{d}{dx} (\theta r)^2 = a - b \left(\frac{\theta^2}{v} \frac{dU}{dx} \right)$$

$$U(\theta^2 r^2)' + b U \theta^2 r^2 = avr^2 \quad (\text{Eq. 17A})$$

$$\frac{d}{dx} (U^b \theta^2 r^2) = avr^2 U^{b-1} .$$

Upon integrating

$$\frac{\theta^2 U}{v} = \frac{a}{r^2 U^{b-1}} \int_{x=0}^x r^2 U^{b-1} dx + C_1 .$$

Using the previous constants, $a = 0.470$ and $b = 6$,

$$\frac{\theta^2 U}{v} = \frac{0.470}{r^2 U^5} \int_{x=0}^x r^2 U^5 dx + C_1 . \quad (\text{Eq. 18A})$$

Equation 18A can be put in dimensionless form by dividing both sides of the equation by $1/r_{eq}$, where r_{eq} is the equivalent radius of the annulus defined at the point of

maximum velocity in laminar flow. This is a quantity used by Knudsen and Katz (23) in annulus studies and corresponds to one-half the hydraulic radius. Further Equation 18A can be multiplied and divided by U_{avg} , where U_{avg} is the average velocity of flow through the annular section. Making these substitutions and re-arranging

$$\left(\frac{\theta}{r_{eq}}\right)^2 N_{eq} = \frac{0.470}{r^2 U^6} \int_0^{\bar{x}} r^2 U^5 d\bar{x} + C_1 ; \quad \bar{r} = \frac{r}{r_{eq}} , \quad \bar{U} = \frac{U}{U_{avg}} ,$$

(Eq. 19A)

$$r_{eq} = \frac{2}{r_t} (r_t^2 - r_{max}^2) ,$$

(Eq. 20A)

$$r_{max}^2 = (r_t^2 - r_h^2) / 2 \ln (r_t / r_h) ,$$

(Eq. 21A)

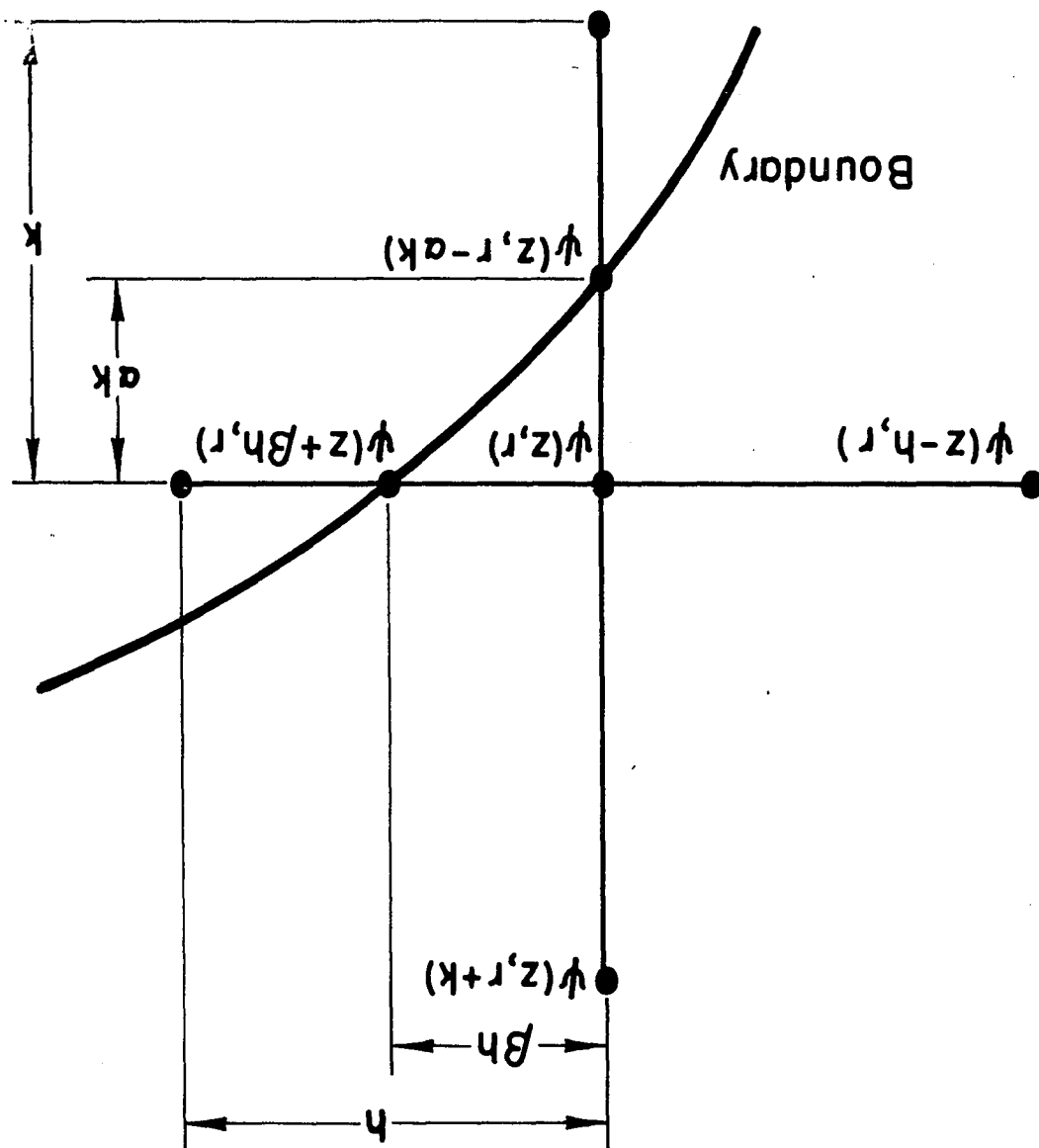
where r_t is the radius to the outside wall of the annulus and r_h is the radius of the inside wall of the annulus. The quantity r_{max} is the radius to the point of theoretical maximum velocity in fully developed laminar flow through an annulus, and $\bar{x} = x/r_{eq}$.

In terms of the above parameters, the second shape factor, Equation 6A, can be reduced to dimensionless form for ease of calculation,

$$K = \left(\frac{\theta}{r_{eq}}\right)^2 N_{eq} \frac{d\bar{U}}{d\bar{x}} .$$

Therefore knowing the momentum thickness distribution, Equation 19A, allows calculation of all of the boundary-layer parameters in terms of the momentum thickness.

Figure 17. Five point mesh used in difference equation



APPENDIX B

Derivation of the Difference Equation
for the Stream Function

The stream function in cylindrical coordinates for the case of axial symmetry is

$$\frac{\partial^2 \psi}{\partial r^2} - \frac{1}{r} \frac{\partial \psi}{\partial r} + \frac{\partial^2 \psi}{\partial z^2} = 0 \quad (\text{Eq. 1B})$$

A five point mesh crossing an irregular boundary was used, see Figure 17. The general difference equation was developed along the lines suggested by Salvadori and Baron (36). The mesh under consideration had spacing of h units in the z direction and k units in the r direction, and α and β are the ratios of the distance to the boundary divided by the regular mesh distance. If the function $\psi(z,r)$ is expanded in a Taylor's series in the r direction, dropping the argument for the derivatives, the following equations result.

$$\psi(z, r+k) = \psi(z, r) + k \frac{\partial \psi}{\partial r} + \frac{k^2}{2!} \frac{\partial^2 \psi}{\partial r^2} + \frac{k^3}{3!} \frac{\partial^3 \psi}{\partial r^3} + \frac{k^4}{4!} \frac{\partial^4 \psi}{\partial r^4} + \dots \quad (\text{Eq. 2B})$$

$$\psi(z, r-\alpha k) = \psi(z, r) - \alpha k \frac{\partial \psi}{\partial r} + \frac{\alpha^2 k^2}{2!} \frac{\partial^2 \psi}{\partial r^2} - \frac{\alpha^3 k^3}{3!} \frac{\partial^3 \psi}{\partial r^3} + \frac{\alpha^4 k^4}{4!} \frac{\partial^4 \psi}{\partial r^4} + \dots \quad (\text{Eq. 3B})$$

If Equation 2B is multiplied by α and the result added to Equation 3B,

$$\frac{\partial^2 \psi}{\partial r^2} = \frac{2\psi(z, r+k)}{k^2(1+\alpha)} + \frac{2\psi(z, r-k)}{k^2\alpha(1+\alpha)} - \frac{2}{k^2\alpha^2} \psi(z, r) + (\alpha^2-1)Ok + Ok^2 \quad (\text{Eq. 4B})$$

where Ok and Ok^2 are terms of the order of k and k^2 respectively.

If Equation 2B is multiplied by α^2 and the result subtracted from Equation 3B, the following is obtained when dividing by r .

$$\frac{1}{r} \frac{\partial \psi}{\partial r} = \frac{\alpha\psi(z, r+k)}{rk(1+\alpha)} - \frac{\psi(z, r-\alpha k)}{rk\alpha(1+\alpha)} + \frac{(1-\alpha)\psi(z, r)}{rk\alpha} + Ok^2 \quad (\text{Eq. 5B})$$

In a similar way,

$$\frac{\partial^2 \psi}{\partial z^2} = \frac{2\psi(z-h, r)}{h^2(1+\beta)} + \frac{2\psi(z+\beta h, r)}{h^2\beta(1+\beta)} - \frac{2}{h^2\beta} \psi(z, r) + (\beta^2-1)Oh + Oh^2 \quad (\text{Eq. 6B})$$

Equations 4B, 5B, and 6B can be substituted in Equation 1B and the result is a difference form of the stream function for the point $\psi(z, r)$ in terms of four surrounding points.

$$\psi(z, r+k) \left(\frac{2}{1+\alpha} \right) \left(1 - \frac{\alpha k}{2r} \right) + \psi(z, r-\alpha k) \left(\frac{2}{1+\alpha} \right) \left(1 + \frac{k}{2r} \right) \left(\frac{1}{\alpha} \right) +$$

$$\begin{aligned} & \psi(z+\beta h, r) \left(\frac{2\lambda^2}{\beta(1+\beta)} \right) - \psi(z-h, r) \left(\frac{2\lambda^2}{1+\beta} \right) - \\ & 2\psi(z, r) \left(\frac{\lambda^2}{\beta} + \frac{1}{\alpha} - \frac{k(1-\alpha)}{2\alpha r} \right) + (1-\beta^2)Oh - (1-\alpha^2)Ok + \\ & Oh^2 + Ok^2 = 0, \end{aligned} \quad (\text{Eq. 7B})$$

where $\lambda^2 = k^2/h^2$, $0 < \alpha \leq 1$, $0 < \beta \leq 1$.

Equation 7B is valid for any mesh point near a boundary. It also applies to an interior point where a change in mesh size is introduced, i.e., the mesh need not be square nor does the mesh have to be regular, that is, k and h need not be the same for every mesh point. For an interior point, $\alpha = \beta = 1$, Equation 7B reduces to

$$\begin{aligned} & \psi(z, r+k) \left(1 - \frac{k}{2r} \right) + \psi(z, r-k) \left(1 + \frac{k}{2r} \right) + \psi(z-h, r) \lambda^2 + \\ & \psi(z+h, r) \lambda^2 - 2\psi(z, r) (1 + \lambda^2) + Ok^2 + Oh^2 = 0. \end{aligned} \quad (\text{Eq. 8B})$$

The error involved is of the order of $(1-\beta^2)h$ in Equation 7B. Care must be exercised to ensure that β does not approach zero. In constructing the net it is necessary to make $(1-\beta^2) \rightarrow h$ if the whole term is to be of the order of h^2 . The same argument holds for α . If the net is made fine enough, $h, k \ll 1$, the terms Oh^2 and Ok^2 tend to zero.

Also it was assumed that all derivatives were bounded. This is, of course, not true at the stagnation point for an elliptic body of revolution. However, if the difference equations do not include this singularity, the unboundedness problem will be avoided.

One more problem should be considered along the lines of discussion presented by Forsythe and Wasow (37). The term

$$1 - \frac{\alpha k}{2r}$$

will be forced positive if

$$\alpha < \frac{2r}{k} .$$

If this latter condition is met and if α , β , k , h , r , are all positive and finite, Equation 7B merely expresses $\psi(z,r)$ as a weighted average of four surrounding points. Since the boundary is specified and is finite and since all derivatives are bounded in the region under consideration, all interior points must be finite.

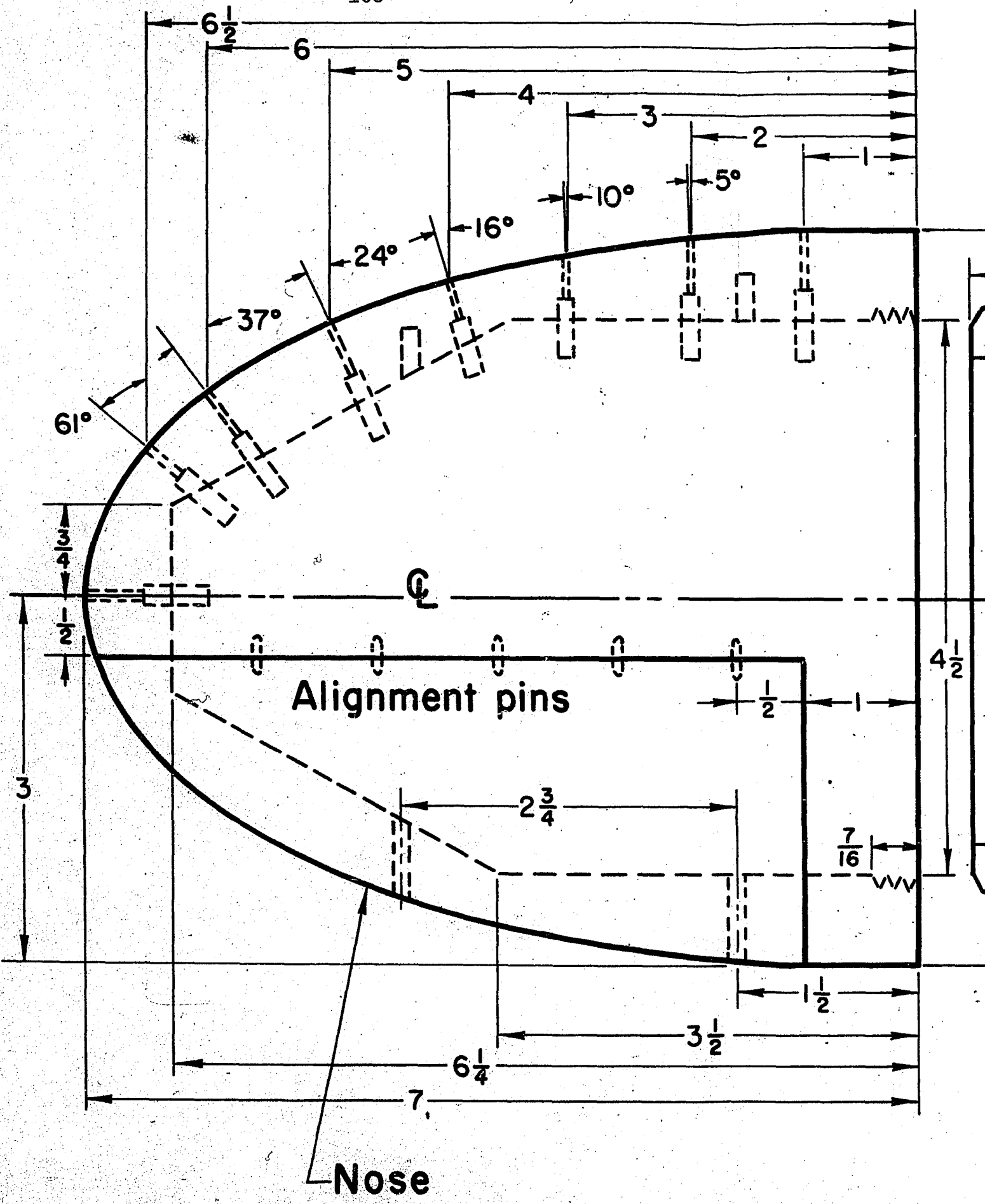
$$0 \leq m \leq \psi(z,r) \leq M \leq \infty$$

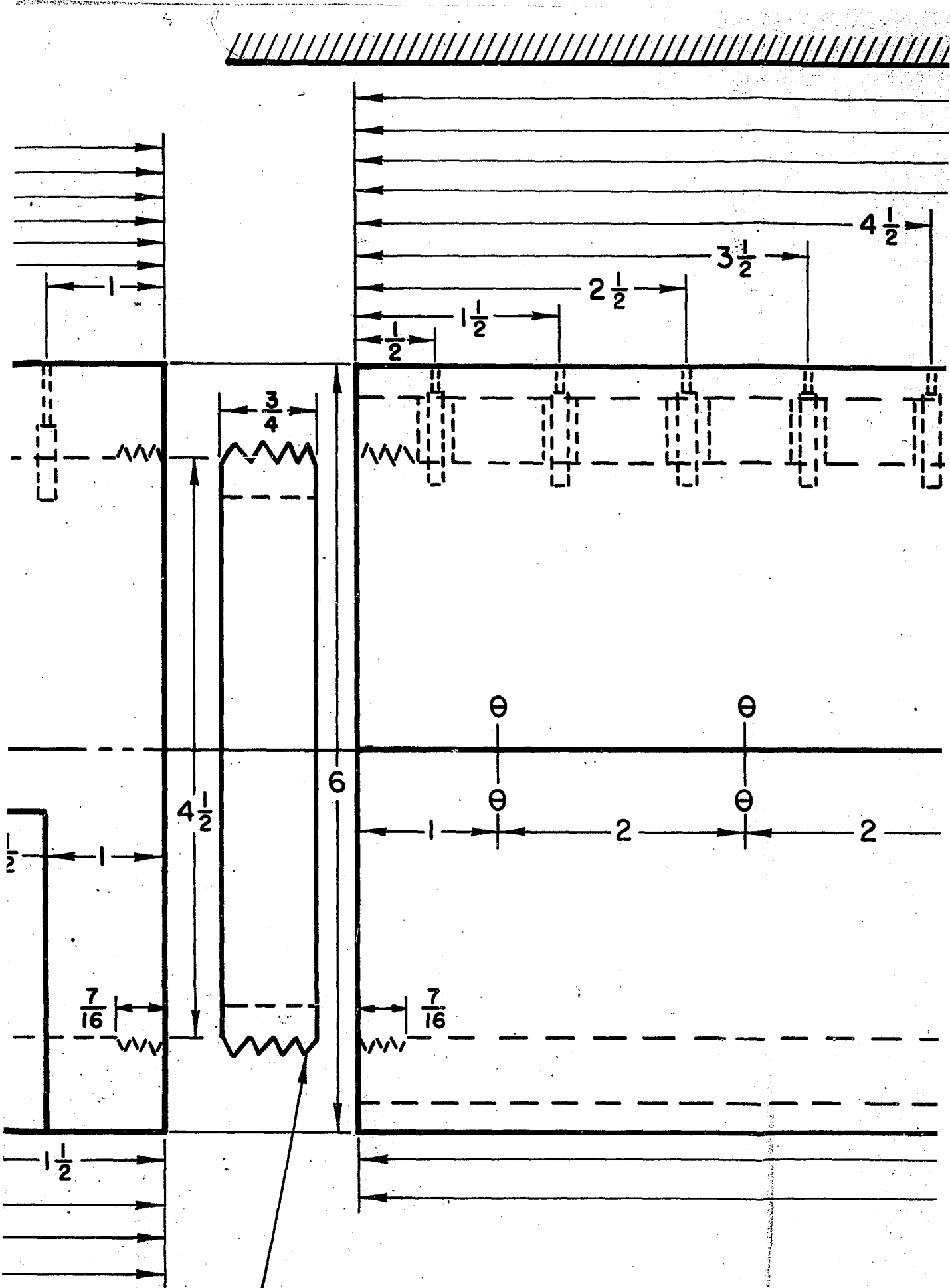
Thus the difference equation should be stable throughout the region interior to the boundary.

APPENDIX C

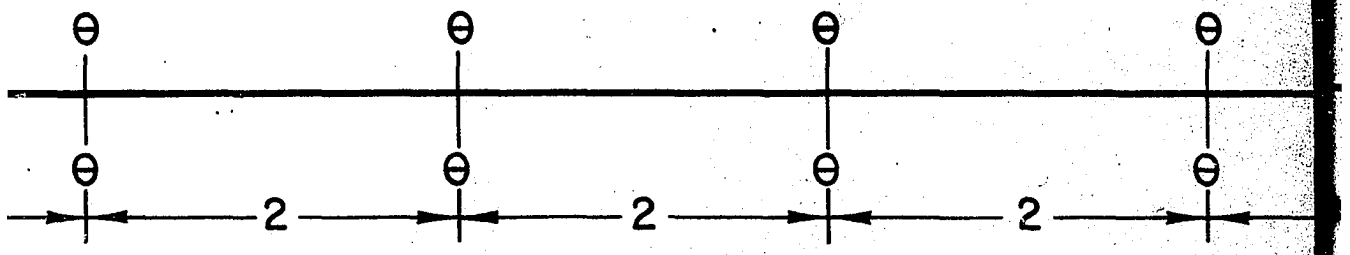
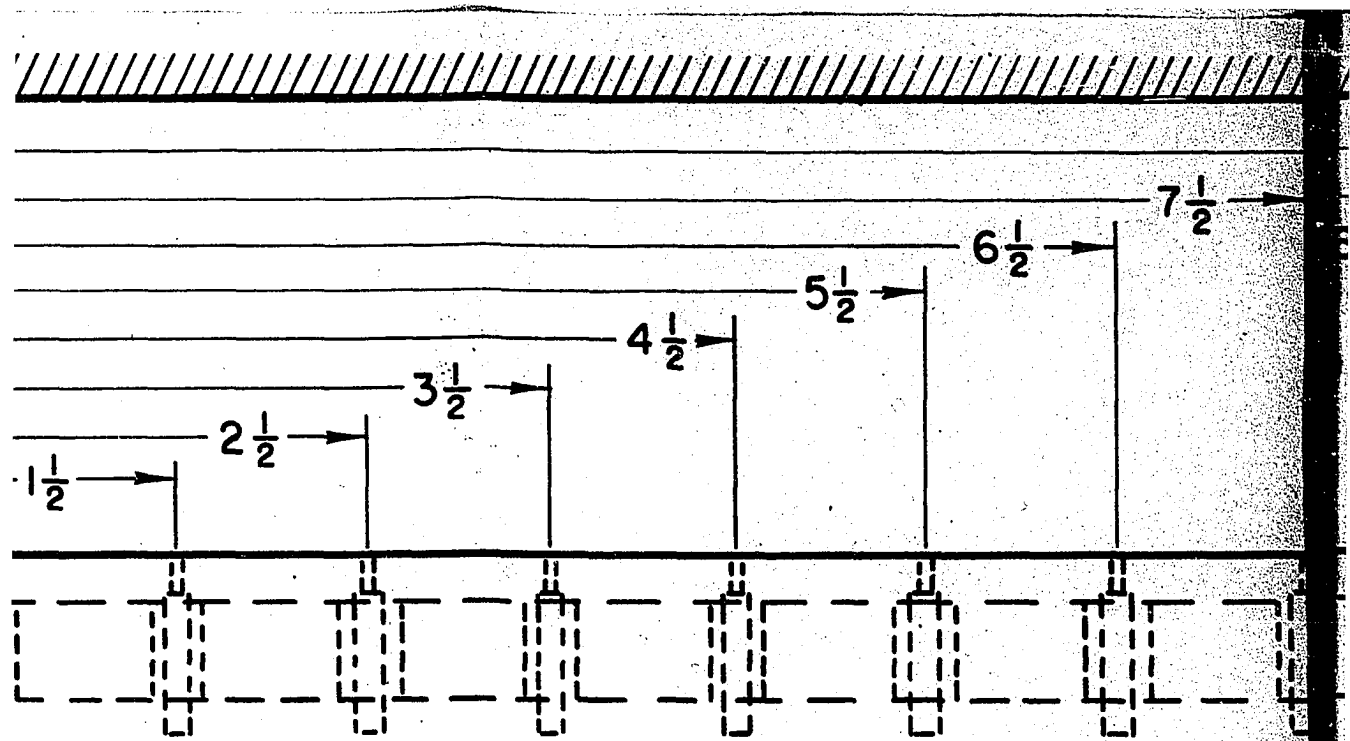
Full Size Drawing of the Model

Figure 18. Full size drawing of the model showing location of static pressure taps

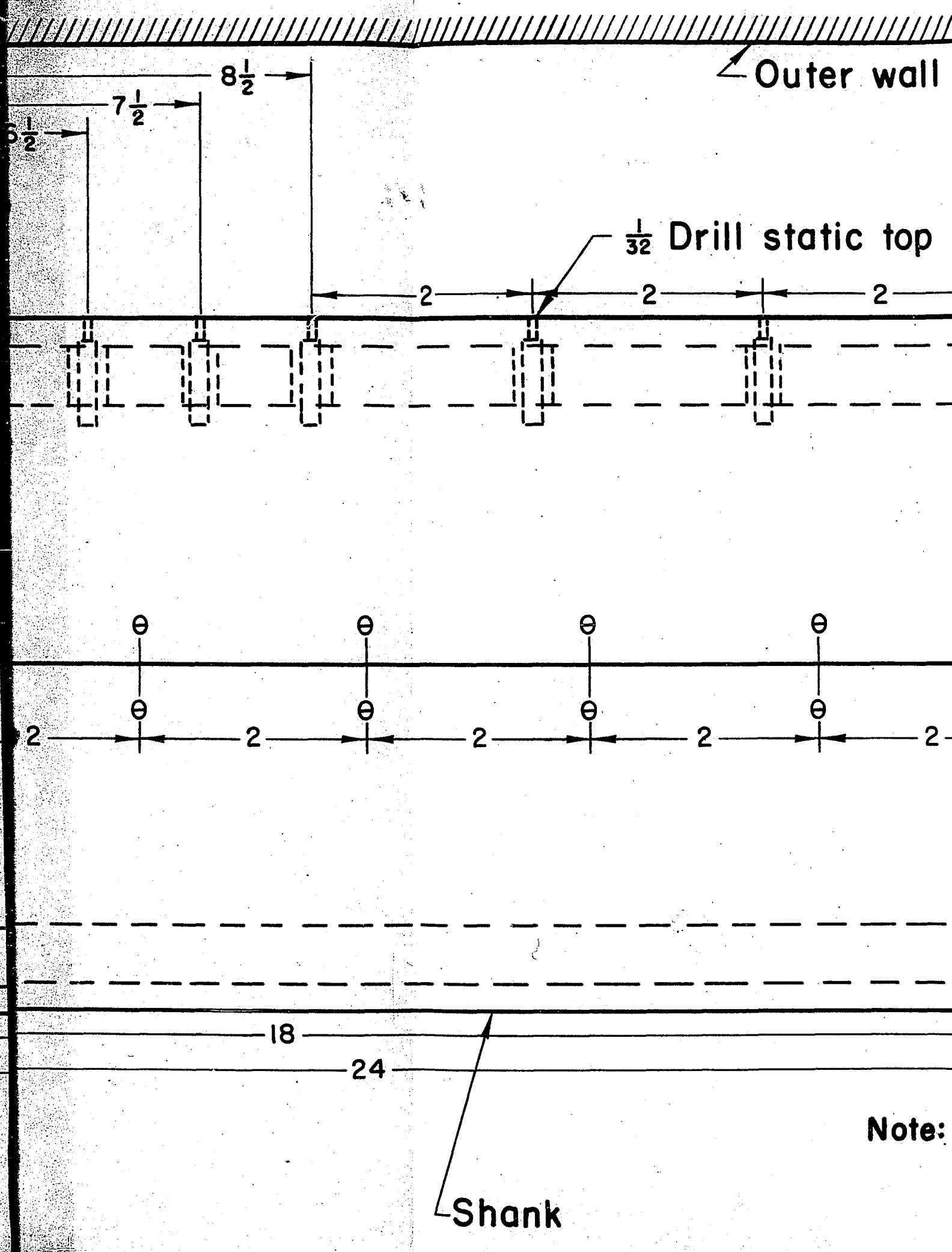




Connector



or



Outer wall

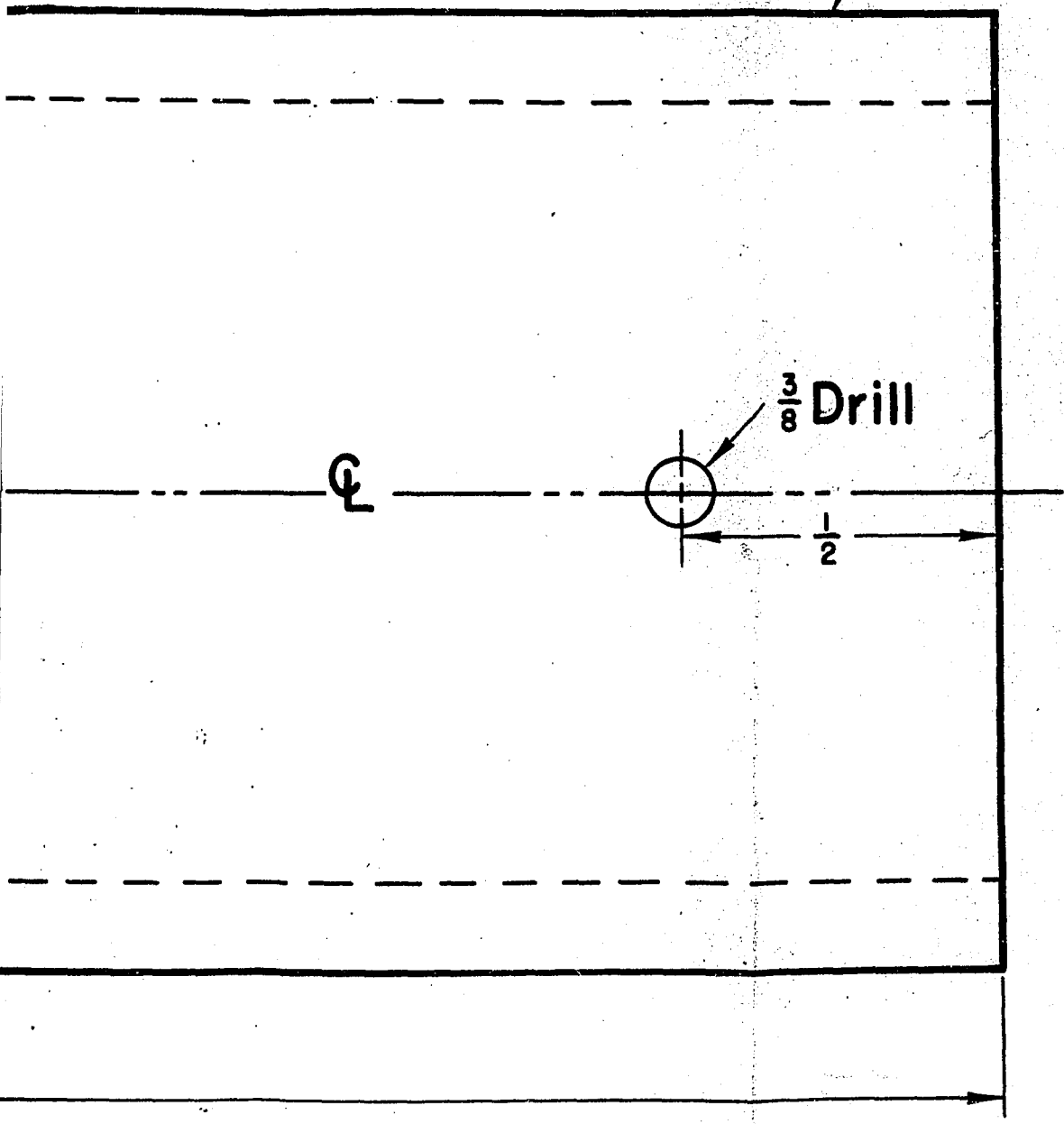
$\frac{1}{32}$ Drill static top

Shank

Note:

pipe

Aluminum tubing $5\frac{1}{2}$ O.D.



hes.